BRNO UNIVERSITY OF TECHNOLOGY

Faculty of Electrical Engineering and Communication

MASTER'S THESIS

Brno, 2022   Bc. Viktória Parobková

BRNO UNIVERSITY OF TECHNOLOGY

VYSOKÉ UČENÍ TECHNICKÉ V BRNĚ

FACULTY OF ELECTRICAL ENGINEERING AND COMMUNICATION

FAKULTA ELEKTROTECHNIKY
A KOMUNIKAČNÍCH TECHNOLOGIÍ

DEPARTMENT OF BIOMEDICAL ENGINEERING

ÚSTAV BIOMEDICÍNSKÉHO INŽENÝRSTVÍ

SEGMENTATION AND MORPHOLOGICAL ANALYSIS OF MOUSE EMBRYO CHOROID PLEXUS

SEGMENTACE A MORFOLOGICKÁ ANALÝZA CHOROIDNÍHO PLEXU MYŠÍHO EMBRYA

SEMESTRAL THESIS
SEMESTRÁLNÍ PRÁCE

AUTHOR   Bc. Viktória Parobková
AUTOR PRÁCE

SUPERVISOR   Ing. Jiří Chmelík, Ph.D.
VEDOUCÍ PRÁCE

BRNO 2022

BRNO **FACULTY OF ELECTRICAL**
UNIVERSITY **ENGINEERING**
OF TECHNOLOGY **AND COMMUNICATION**

Master's Thesis

Master's study program **Biomedical Engineering and Bioinformatics**

Department of Biomedical Engineering

Student:	Bc. Viktória Parobková	***ID:***	203681
Year of study:	2	***Academic year:***	2021/22

TITLE OF THESIS:

Segmentation and morphological analysis of mouse embryo choroid plexus

INSTRUCTION:

1) Get acquainted with the anatomy and morphology of the mouse embryo brain, and with its imaging using X-ray computer microtomography. 2) Carryout literature research of segmentation methods suitable for segmentation of the choroid plexus of the fourth ventricle in CT image data. 3) According to the performed review, select a suitable segmentation method and implement it in any programming environment. 4) Test the implemented method on the available data and optimize the segmentation method. 5) Propose suitable morphological features of segmented formations and create a software for their calculation. 6) Carry out a morphological analysis on the available data, statistically evaluate the achieved results and discuss it appropriately.

RECOMMENDED LITERATURE:

[1] JAN, Jiri. Medical Image Processing, Reconstruction and Analysis: Concepts and Methods. Second Edition. Boca Raton: CRC Press, 2019. ISBN 9781138310285.

[2] HUBERT, Violaine, Fabien CHAUVEAU, Chloé DUMOT, Elodie ONG, Lise-Prune BERNER, Emmanuelle CANET-SOULAS, Jean-François GHERSI-EGEA a Marlène WIART. Clinical Imaging of Choroid Plexus in Health and in Brain Disorders: A Mini-Review. Frontiers in Molecular Neuroscience. 2019, 12. ISSN 1662-5099. DOI 10.3389/fnmol.2019.00034.

Date of project specification:	7.2.2022	***Deadline for submission:***	20.5.2022

Supervisor: Ing. Jiří Chmelík, Ph.D.

prof. Ing. Ivo Provazník, Ph.D.
Chair of study program board

ABSTRACT

The Choroid Plexus is a regulated gate between blood and cerebrospinal fluid and takes place in several functions connected with the neural system. However, many functions are still unknown caused by the fragility, location and shape of the plexus. Thus the noninvasive techniques are used to access this crucial brain component located within the ventricles. Moreover, there is a link between its shape and brain pathologies. This project aimed to extract the ChP of the 4th ventricle by implementing segmentation methods followed by morphological analysis to discover patterns between the shape and disease.

KEYWORDS

Choroid Plexus, Fourth Ventricle, Image Segmentation, Brain, micro-CT, morphological analysis

ABSTRAKT

Choroidálny plexus je regulovanou bránou medzi krvou a mozgovomiechovým mokom a má niekoľko funkcií spojených s nervovým systémom. Mnohé funkcie sú však stále neznáme, čo je spôsobené krehkosťou, umiestnením a tvarom plexu. Preto sa na prístup k tejto kľúčovej súčasti mozgu, ktorá sa nachádza v komorách, používajú neinvazívne techniky. Okrem toho existuje súvislosť medzi jeho tvarom a patologickými stavmi mozgu. Cieľom tohto projektu bolo extrahovať ChP 4. komory implementáciou segmentačných metód a následnou morfologickou analýzou s cieľom odhaliť zákonitosti medzi tvarom a ochorením.

KĽÚČOVÉ SLOVÁ

Choroidálny plexus, štvrtá komora, segmentácia obrazu, mozog, mikro-CT, morfologická analýza

ROZŠÍRENÝ ABSTRAKT

Choroidálny plexus (ChP) je vysoko vaskularizované tkanivo, ktoré sa nachádza v štyroch mozgových komorách - laterálnej, tretej a štvrtej komore. ChP sa podieľa najmä na produkcii mozgovomiechového moku (cerebrospinal fluid - CSF) tým, že využíva voľný prístup do krvného kompartmentu netesných ciev. Pozostáva z viacerých typov buniek vrátane: epitelových, endotelových, mezenchýmových a imunitných buniek. Na oddelenie krvného a CSF kompartmentu tvoria epitelové bunky choroidálneho plexu bariéru medzi krvou, CSF a mozgom. ChP je v neurovede málo preskúmanou oblasťou, ale priťahuje čoraz viac pozornosti, pretože sa postupne osvetľuje jeho vývojová funkcia a čoraz viac sa upozorňuje na jeho úlohu v neuropatológii. Nedávno sa ukázalo, že zloženie CSF a faktory odvodené od ChP, ako sú signálne a trofické molekuly, zohrávajú nezastupiteľné funkcie pre vývoj mozgu, homeostázu mozgu a niky dospelých neurálnych kmeňových buniek. Zmeny v štruktúre a funkcii ChP-CSF sa spájajú s neurodegeneratívnymi ochoreniami, ako je Alzheimerova choroba, s neurovývojovými poruchami, poruchy autistick-ého spektra a schizofrénia, a tiež s neuroimunitnými ochoreniami, ako je skleróza multiplex. [30] [18] [35] [53]

Cieľom semestrálnej práce je štúdium myšieho modelu straty funkcie génov Cdk13 a Tmem 107 a kontrolných myší (wt) pomocou morfologickej analýzy choroidálneho plexu v dátach z mikro-CT. Pretože podľa predbežných výsledkov vykazujú myši s mutovaným génom Cdk13 výrazné morfologické zmeny v ChP.

V prvej časti práce je opísaná anatómia a morfológia embryonálneho mozgu myší. Na prístup k morfológii cievnatého plexu boli diskutované segmentačné prístupy s cieľom vybrať vhodný algoritmus na detekciu cievnatého plexu v rámci mikro CT údajov.

Metodická časť práce je zameraná na vývoj nástroja na komplexnú morfologickú analýzu ChP u mutovaných a wt myší. Segmentácia ChP je potrebná na umožnenie akejkoľvek morfologickej analýzy. Na základe dostupných metód na segmentáciu ChP bola vybraná a implementovaná jedna metóda.

Choroidálny plexus sa nachádza v štvrtej komore a prebieha pozdĺž jej zadnej dolnej steny [16]. Hlavnou myšlienkou segmentácie choroidálneho plexu je teda najprv segmentovať oblasť komory, čo umožňuje lokalizáciu plexu v zobrazovacích dátach mozgu. Segmentácia komôr na základe modelu [29] a porovnávanie šablón [9] sú metódy určené na segmentáciu komôr. QIAN a kol. [37] zaviedli jednoduchú metódu na segmentáciu komôr v údajoch µCT, ktorá nevyžaduje predchádzajúcu znalosť modelu komôr ani ich šablóny. Rozpoznávanie CSF na CT snímkach je založené na jej intenzite, ktorá je nižšia ako v prípade ostatných mozgových tkanív [28] [15]. Preto sa na rozlíšenie tkaniva od CSF používa prahovanie. Najprv sa objem prahuje pomocou prahu určeného Otsuovou metódou, čím sa vytvorí maska tkaniva.

Potom sa na masku aplikuje morfologické uzavretie, aby sa vytvorila nová maska, ktorá zahŕňa tkanivo a CSF. Následne sa CSF extrahuje odčítaním tkanivovej masky od morfologicky uzavretej masky. Výsledkom sú oblasti CSF a výberom najväčšieho spojeného segmentu je získaná maska štvrtej komory.

Segmentácia choroidálneho plexu je založená na jeho umiestnení v komore [16] [4]. Preto sa použila extrahovaná maska komory. Maska zahŕňala len oblasti s CSF a nie choroidálny plexus. Na masku komory sa použilo morfologické uzavretie, aby zahŕňala aj plexus. Na extrakciu cievnatého plexu z komory sa použilo prahovanie na voxely v maskovaných oblastiach. Týmto prístupom sa segmentovala len časť oblasti plexu. Pre pridanie zvyšných voxelov do konečnej masky choroidálneho plexu boli použité aktívne kontúry. V poslednom kroku, boli artefakty odstránené nastavením nulovej hodnoty voxelov nad maskou štvrtej ventrikuly. Odstránenie sa vykonalo v koronálnej rovine (teda v 2D) a len v oblasti nad maskou, pretože v tejto oblasti nie je plexus spojený so stenou komory. Artefakty v oblasti pod komorovou maskou boli odstránené manuálne v programe AVIZO. Chýbajúce časti plexu, ktoré neboli vysegmentované vyššie popísaným postupom boli manuálne dosegmentované. Jedná sa o laterálne oblasti plexu, ktoré siahajú do Luschkoveho otvoru. Tieto oblasti sú v niektorých prípadoch ťažko odlíšiteľné od okolitého tkaniva kvôli malému kontrastu.

V ďalšej časti práce bola prevedená kvantitatívna a morfologická analýza vysegmentovaných modelov s cieľom porovnať rozdiely medzi Cdk13 a Tmem 105 vzorkami a mutantami so vzorkamki kontrolných myší. Objem, povrch a uhol, pod ktorým rastie ChP do komory boli vyhodnotené. Analýza tvaru modelu bola prevedená pomocou GPA (Generalized Procrustes Analysis [47]), ktorá bola aplikovaná na manuálne vybrané body na modely (landmarks). Metóda je založená na výpočte priemerného modelu. Ostatné modely sú s ním následne zarovnané pre výpočet Prokrustovej vzdialenosti. Vzdialenosť bola stanovená medzi jednotlivými vzorkami a priemerným modelom, a medzi dvojicami vzoriek.

Výsledky analýzy sú následne popísané. Choroidálny plexus rastie u rôznych organizmov rôzne [22]. Preto sa očakávalo, že pre každý model bude mať iné parametre.

Výsledky boli porovnávané medzi skupinami (Cdk13, Tmem 105), 13- (E13) a 15-dňovými (E15) embryami a medzi mutantami a kontrolnými vzorkami. Najskôr sa ukázalo, že všetky modely Cdk13 E13 majú nespojené vertexy v RSS (rostrálny sagitálny segment), a chýbalo im predĺženie do Luschkovho otvoru. Po druhé, objem a povrch ukázali, že ich hodnoty sú proporcionálne, ako sa očakávalo. Celkovo vzorky E13 vykazovali nižšie hodnoty objemu a povrchu ako E15. Skupina Tmem má výraznejší objem a povrch ako skupina Cdk13. Vzorky Cdk15 vykazovali väčšiu priemernú hodnotu pre kontrolné vzorky, zatiaľ čo mutanti mali väčší priemerný objem a povrch v rámci skupiny Tmem.

Okrem toho sa objem a plocha povrchu medzi mutantami a kontrolnými vzorkami výrazne nelíšia. Najmenšia hodnota však bola nameraná pri vzorkách mutantov a najvyššia pri modeli kontrolnej vzorky. Preto typ vzorky (mutant/kontrolná vzorka) a objem/povrchová plocha nie sú korelované.

Ďalej sa analyzoval uhol rastu. Choroidálny plexus rastie pod tupým alebo ostrým uhlom. Všetky vzorky Cdk13 majú tupý uhol rastu, zatiaľ čo ostrý uhol možno pozorovať v rámci skupiny Tmem s výnimkou dvoch modelov, ktoré majú uhol mierne nad 90°. Opäť nie je významný rozdiel medzi rastovými uhlami mutantov a kontrolnými vzorkami.

Nakoniec sa analyzoval tvar segmentovaných modelov zarovnaním bodov (landmarks) k odhadnutému priemernému tvaru. Prokrastova vzdialenosť potom ukázala odlišnosť modelov od priemerného tvaru a medzi sebou navzájom. Celkovo sa tvary líšia medzi vzorkami rôzneho druhu a embryonálneho veku. Najväčšiu vzdialenosť od priemerného tvaru vykazoval mutant E13 Cdk13 a najmenšia vzdialenosť bola odhadnutá pre kontrolnú vzorku zo skupiny Tmem. Vzdialenosť od priemerného tvaru je vyššia v rámci mutantov ako v prípade kontrolných vzoriek. Porovnanie jednotlivých dvojíc modelov odhalilo väčšiu vzdialenosť medzi mutantami ako medzi kontrolnými modelmi v rámci skupiny Tmem. Vzorky E13 Cdk13 vykazovali opačné výsledky. Nakoniec bolo vykonané zhlukovanie a PCA pre štatistické vyhodnotenie rôznorodosti modelov. Výsledky ukázali rozdiel medzi vzorkami Cdk13 a Tmem. Preto sa modely tej istej skupiny pôvodne zhlukovali spolu, s výnimkou jednej dvo-jice, kde sa vzorka Cdk13 zhlukovala s modelom Tmem. Celkovo zhluková analýza nevykazovala rozdiely medzi kontrolnými vzorkami a mutantami. PCA rozdelila vzorky pozdĺž PC2 do zhluku Tmem a Cdk13. V zhluku Cdk13 sú však zahrnuté dve odľahlé hodnoty zo skupiny Tmem. Okrem toho sú modely E13 Cdk13 viac vzdialené od ostatných modelov. Nakoniec PCA ukázala vzťah medzi kontrolnými vzorkami a mutantami v rámci skupiny Tmem, kde sú vzorky rovnakého druhu (mutant/kontrolná vzorka) v blízkej vzdialenosti.

Author's Declaration

Author:	Bc. Viktória Parobková
Author's ID:	203681
Paper type:	Master's Thesis
Academic year:	2021/22
Topic:	Segmentation and morphological analysis of mouse embryo choroid plexus

I declare that I have written this paper independently, under the guidance of the advisor and using exclusively the technical references and other sources of information cited in the paper and listed in the comprehensive bibliography at the end of the paper.

As the author, I furthermore declare that, with respect to the creation of this paper, I have not infringed any copyright or violated anyone's personal and/or ownership rights. In this context, I am fully aware of the consequences of breaking Regulation § 11 of the Copyright Act No. 121/2000 Coll. of the Czech Republic, as amended, and of any breach of rights related to intellectual property or introduced within amendments to relevant Acts such as the Intellectual Property Act or the Criminal Code, Act No. 40/2009 Coll. of the Czech Republic, Section 2, Head VI, Part 4.

Brno   . . . .
author's signature*

---

*The author signs only in the printed version.

ACKNOWLEDGEMENT

Contents

List of Figures

List of Tables

Introduction

Choroid plexus (ChP) is a highly vascularized tissue located within the four brain ventricles - lateral ventricle, third ventricles, and fourth ventricle. ChP is mainly involved in the production of cerebrospinal fluid (CSF) by using the free access to the blood compartment of the leaky vessels. It is comprised of multiple cell types, including: epithelial, endothelial, mesenchymal and immune cells. In order to separate blood and CSF compartments, choroid plexus epithelial cells constitute the blood–CSF–brain barrier. ChP is an understudied area in neuroscience but it is attracting more attention as its developmental function is gradually illuminated and its role in neuropathology is increasingly noticed. Recently, it has been demonstrated that CSF composition and ChP-derived factors, such as signalling and trophic molecules, play indispensable functions for brain development, brain homeostasis and adult neural stem cell niches. Interestingly, changes in ChP-CSF structure and function have been linked to neurodegenerative diseases such as Alzheimer's disease, to neurodevelopmental disorders such as autism-spectrum disorder and schizophrenia and also to neuroimmune disease such as multiple sclerosis. [30] [18] [35] [53]

The semestral thesis aims to study the mouse model for loss of function of Cdk13 and Tmem 107 genes and the control wild-type (wt) mice by morphological analysis of the choroid plexus in the micro-CT data. Because, in the preliminary results, the mice with the mutated Cdk13 gene displays distinctive morphological changes in ChP.

In the first part of the thesis, the anatomy and morphology of the embryonic mouse brain will be described. To access the morphology of the choroid plexus, the segmentation approaches will be discussed to choose a proper algorithm for the detection of the choroid plexus within the micro CT data.

The methodical part of the thesis will be focused on developing a tool for complex morphological analysis of ChP in mutant and wt mice. Segmentation of the ChP is required to enable any morphological analysis. Based on the available methods for ChP segmentation, one method was selected and implemented. The analysis of the segmented models will be done quantitatively and morphologically to study the differences among the different types of samples. First, the volume, surface area, and growth angle will be computed. Then the shape alterations will be analyzed using the Generalized Procrustes Analysis. Finally, the segmentation and model analysis results will be discussed, and the method limitations will be summarized. The results of different sample types and kinds will be compared.

Aim of the thesis

During the prenatal and neonatal stages, the mammalian brain grows rapidly. In the adult stage, structural changes are critical for normal brain functions. The main functions are from creating fundamental functional units and neural circuits to axonal pruning and myelination. Advanced imaging methods could examine the growing brain from macroscopic to microscopic levels, exploring normal and abnormal changes. [53]

The laboratory mouse has been widely used as a model organism to investigate the genetic regulatory mechanisms of brain development and the relationship between insult and pathology. Over the last decade, mouse brain development has also been a significant focus of neuroscience research. As a result, imaging tools are frequently used to help understand the brain on a higher level. [53]

This thesis will focus on an essential part of the brain named the choroid plexus (ChP), responsible for producing cerebrospinal fluid (CSF). CSF serves as a fluid cushion and a sink for waste from the neurological system in vertebrates. The ChP-CSF system also influences the regulation of neural stem cells and overall the normal functioning and development of the nervous system. The ChP studies have also revealed its ability to release a wide range of bioactive chemicals that regulate processes over the entire central nervous system via CSF. Moreover, ChP has been identified as a sensor that reacts to CSF composition modifications connected with CNS activity patterns changes. [30] [18] [35]

The link between the morphology of ChP and human brain pathologies has been recently discovered (schizophrenia, epilepsy and Alzheimer's disease). Thus the choroid plexus studies can stimulate new ambitions for treating neurological disease. Still, many of its functions remain unknown, caused by its deep location within the brain and its fragility. Therefore a non-invasive investigation is required. [30] [18] [35] [53]

1 Anatomy and morphology of embryonic mouse brain

Before and after birth, critical events in mouse brain development occur, starting with peak neurogenesis of the cranial motor nuclei nine days after conception and ending with eye-opening 30 days after conception.

Briefly, the embryonic mouse brain development will be described. The two most fundamental of them are cerebral white and cerebral grey. In the early days, cranial motor nuclei, inferior olivary nucleus, and Purkinje cells have a peak day of neurogenesis between E9-E10.5. Furthermore, the ventricles are developing at E9.5. Around E11, the cranial sensory and retinal nuclei are formed along with the medial and ventrolateral geniculate nucleus, globus pallidus and subplate. Next, the cochlear nuclei, lateral geniculate nucleus, amygdala and mitral cells are formed at E12. The epithalamus, thalamus, and hypothalamus differentiate from the diencephalon by E12. By E12.5, ventroposterolateral and ventrobasal nuclei have a peak day. To this day, the structures of the preoptic nucleus, claustrum, nucleus of the lateral olfactory tract, and cortical layer VI are developed. During E13-E13.5, the pontine and septal nuclei, raphe complex, superior colliculus, suprachiasmatic and anterior olfactory nucleus, subiculum, entorhinal cortex, retinal ganglion cells, and lastly, the cortical layer V have a peak of neurogenesis. The caudoputamen and cones are formed at E14. At E15, the retinal amacrine cells and the cortical layer II-III are developed. Furthermore, between E16-E17, the isles of Calleja, the nucleus accumbens, tufted cells, and cortical layer IV are experiencing the peak day. Lastly, the rods are formed at E19.

This work will focus on the choroid plexus, which arises during E12.5-E13 and develops within the lateral, third and fourth ventricles. The choroid plexus of the fourth ventricle originates from the roof plate and the rhombic lip. The choroid plexus is extensive within the lateral ventricles and the fourth ventricle at the stage of E13.5-15.5, while the plexus of the fourth ventricle is the largest. By E16.5, the plexus has expanded to all areas where it can be found in the adult. [11] [14] [8]

1.1 Choroid Plexus

There is a choroid plexus within each brain ventricle - fourth ventricle (Hindbrain ChP), lateral ventricles (Telencephalic ChP), and third ventricle (Diencephalic ChP). More precisely, it is found in the roofs of the third and fourth ventricles and in the temporal horns of the lateral ventricle as it shown in figure 1.1. [35] [30] It is

formed by vascular pial stroma covered by a choroidal epithelium and contains fenestrated vascular endothelium. The secretory role of the choroid plexus is reflected in its structure. Stromal core of capillaries and connective tissue is surrounded by a monolayer of cuboidal epithelial cells. The blood-CSF barrier is formed by adjacent ChP epithelial cells which are bound together by tight junctions. This barier prevents the leakage of moleculs from the blood ciculation into the CSF. Furthermore, the tight junctions helps to secure the apico-basal polarity of membrane proteins that are important for normal epithelial cell function. The blood–CSF barrier alters throughout development, providing differential neuroprotection or CSF synthesis control in the embryonic versus the adult brain. The blood reaches the plexus from either the anterior or posterior ciculation into the choroid. [30] [18] Thus, the ChP is a crucial part of the brain as its primary function is the secretion and production of cerebrospinal fluid. [50] Many functions are still unknown, which is caused by the location, fragility and shape of plexus. Morphological changes can be a result or lead to multiple disorders like Alzheimer's Disease. Thus there is a link between ChP shape and brain pathologies. [24]
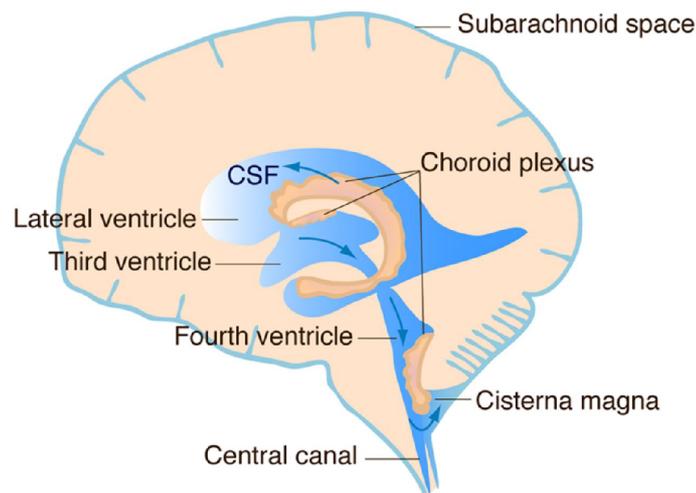
Fig. 1.1: Ventricles of the brain. The lateral, third and fourth ventricle are shown within this figure in blue. The arrows represent the CSF secretion and flow. The CSF is secreted by the choroid plexus (orange) and flows from the lateral ventricles to the third and fourth ventricles. The big part of the CSF drains into the subarachnoid space through foramens. The rest of the CSF is ending in the central canal. [27]

1.1.1   Choroid Plexus of 4th ventricle

The three types of ChP occur within a brain, and its shape depends on location. This thesis will focus on the anatomy of the fourth ventricle ChP, as only few studies

have been performed on its morphology [52]. The location of the choroid plexus of fourth ventricle is shown in figure 1.2.

Fig. 1.2: Sagittal view of the choroid plexus of the fourth ventricle (arrow). [52]

The ChP of the fourth ventricle is placed along the inferior posterior wall of the ventricle and has a bulky and lobulated shape and has two arms growing from the tela choroidea and extending into the ventricular cavity via foramina of Luschka. These branches form two cauliflower-like masses and are called Bochdalek's flower baskets. The tela choroidea forms the ceiling of the bottom part of this ventricle. Plexus consists of highly branching vascularized tufts. Tufts are thin-walled and epithelial cells containing long bulbous microvilli on the luminal surface. [48], [52]

The figure 1.3 shows that plexus can be divided into rostral and caudal sagittal segments (RSS, CSS) and medial and lateral horizontal segments (MHS, LHS). The boundaries between RSS and CSS are not as visible as between LHS and MHS and between MHS and RSS. [35]

MHS elongates from the core of the inferior half of the roof to the caudal vermis through the foramen of Magendie. LHS project outwardly among the vestibulo-cochlear nerve's roots on the superior side and the glossopharyngeal nerve on the inferior side. This segment lengthens from the rostral edge of the MHS into the cerebellopontine angle. The LHS extends into the foramen of Luschka. At the level of the foramen of Magendie, the CSS attenuate, and the epithelial roof from whence this segment arises is in touch with the cerebellum's undersurface. [16], [48], [52]

CSF production, development, and maintenance of the periventricular neurogenic zones, neuroimmune transmission, and delivery of micronutrients, growth factors, hormones, and neurotrophins to the brain via the CSF, either from systemic

blood through the leaky microvasculature or from the CP epithelium or mesenchymal components, are all important functions of the CP. Only two of these functions are completed by the plexus during the development, the blood-CSF barrier and CSF regulation. [20] [35]
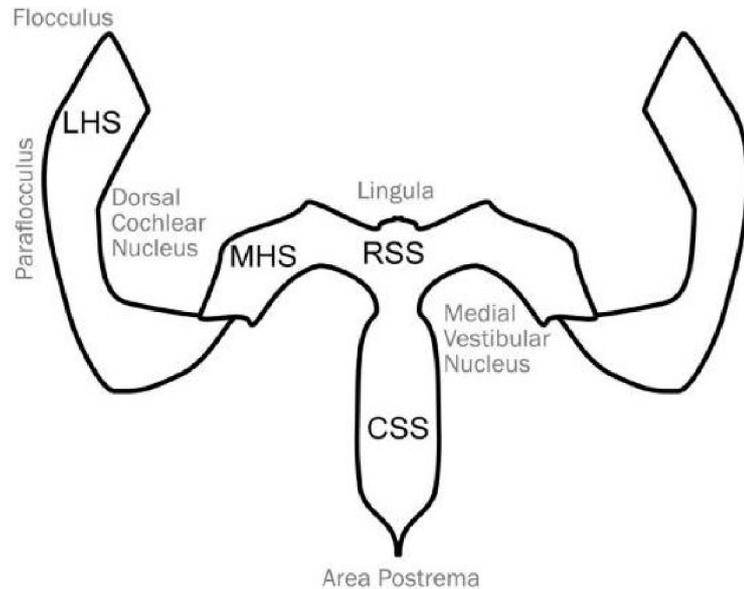
Fig. 1.3: Choroid plexus divided into 4 segments. RSS, rostral sagittal segment; CSS, caudal sagittal segment; MHS, medial horizontal segment; LHS, lateral horizontal segment.[35]

1.2 Cerebrospinal fluid system

CSF is an ultrafiltrate of plasma in the brain ventricles and the subarachnoid spaces of the skull and spine. Its primary function is providing nourishment, removing metabolic waste and protecting the brain. The fluid is produced within the ventricles. The CSF system comprises of ventricles, cisterns and subarachnoid space (SAS). These areas are connected in series. The CSF flow is showe in figure 1.4. First, CSF generates in lateral ventricles and than flows to the third ventricle through the foramina of Monro. Next, the fluid flows to the fourth ventricle via the foramen of Magendie and foramen of Luschka. Finally, fluid flows into the subarachnoid space and is reabsorbed at the dural venous sinuses and around the neural sheaths. The ventricles will be further described as the production of CSF takes place within these regions. [24]
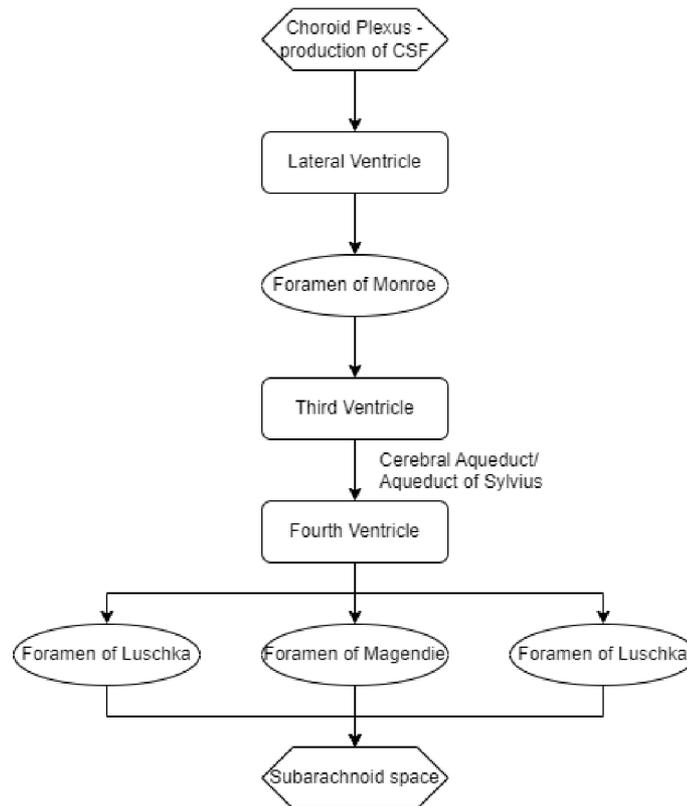
Fig. 1.4: CSF flow in the brain. The CSF is formed by choroid plexus and drains into subarachnoid space via foramens or is ending in central canal. [27]

Lateral ventricles

Lateral ventricles are posteriorly in contact with the thalamus, laterally surrounded by cerebral white matter and superiorly bounded by the corpus callosum and forceps. The medial portion near the temporal horns is joint to the amygdala. [24]

Foramina of Monro

ChP and thalamus surround posterior and lateral sides of the foramina of Monro. By coursing anteriorly along the choroidal fissure, the ChP reaches the inferolateral aspect of this area. [24]

Third Ventricle

The third ventricle is laterally surrounded by the thalami and is close to the hypothalamus on its anteroinferior border. The ChP of the lateral ventricle extends into the third ventricle through the foramina of Monro. This ventricle includes

internal cerebral veins, which drain ChP and merge into the great cerebral vein. [24]

Cerebral Aqueduct

It is enclosed by the periaqueductal grey matter of the midbrain. The third and the fourth ventricles are attached to the cerebral aqueduct. [24]

Fourth Ventricle
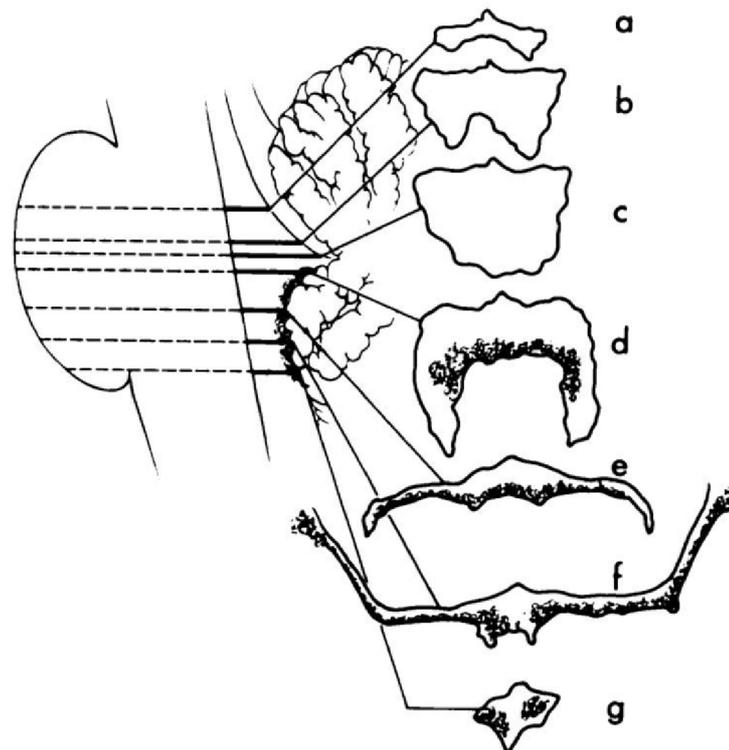
Fig. 1.5: Serial cross section of fourth ventricle. View of individual slices: axial plane. Choroid plexus can be recognized in d through g as a darker region within the ventricle. [16]

The 4th ventricle is a part of the brain's ventricular system and is surrounded anteriorly by the pons and medulla, posteriorly by the cerebellum and inferiorly by the spinal canal and spinal cord. Among the ventricles, the fourth ventricle is placed the most inferiorly. It prolongs from the cerebral aqueduct until the central canal of the spinal cord. Superiorly, the 4th ventricle is linked with the third ventricle via the cerebral aqueduct of Sylvius. The CSF drains into the surrounding tissue through the foramen of Luschka at superolateral portions of the ventricle and through the

foramen of Magendie at inferomedial portions. The rest of the CSF which is not drained thought these canals goes into the central canal of the spinal cord. [42] The structure of the fourth ventricle is shown in figure 1.5. It is possible to see that it has a complex configuration. [16]

2 μCT in the visualisation of embryonic mouse brain

X-ray micro-computed tomography (μCT) is a promising technology for visualising mineralised tissue and enables a 3D imaging of biological objects with a resolution within a micrometre scale. The resolution can go down to 1 μm and is dependent on the size of the sample. A native computed tomography's limitation of soft tissue analysis is a low contrast of this tissue within an obtained image. A sample staining can enhances low contrast. [34]
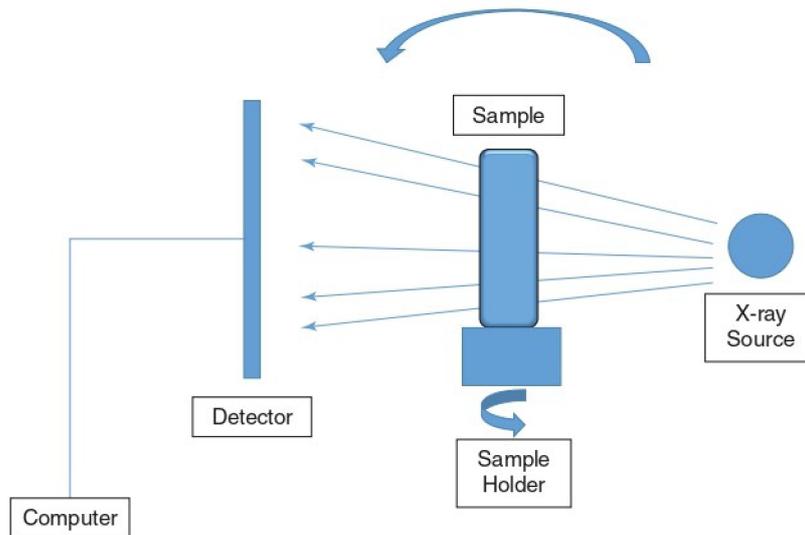
Fig. 2.1: Components of the micro-CT. [34]

The X-ray micro-computed tomography (μCT) system comprises an X-ray generator, sample stage, detector, CCD camera and filters. A sample is placed within a stage between an X-ray generator and detector, as shown in the figure 2.1. The stage enables sample rotation which is crucial in 3D imaging. The X-rays pass through the sample where they are attenuated and then are captured by the detector. Attenuation defines the sample density at the exact point. The scintillator in the top layer of the detector then converts the X-rays into visible light, which enables the detection on the CCD camera. The 2D projection is taken at each sample rotation. A reconstruction software then processes the set of the projections using a filtered back-projection and creates a 3D Image stack. Higer number of projections can maximise shape accuracy. [34]

2.1 Staining

Contrasting agents are required to increase the X-ray absorption of soft tissues. Various methods for staining biological samples are available. Phosphotungstic acid (PTA) is frequently used to improve the contrast of soft tissue. It has a remarkable ability of contrast improvement once the PTA is attached to proteins such as collagens and fibrils. [51]

There are different staining protocols and chemicals to increase the X-ray absorption by distinct tissues. In addition to PTA, Iodine, silver, or iron stains are used for contrast improvement. Sample preparation with Iodine stain is done by two steps sample dehydration using ethanol grade (80%, 100%). Then the sample is placed in I2E (stock solution of 1% iodine in 96% alcohol). The PTA staining is very similar. The specimen is dehydrated in 70% ethanol and then stained in a 30 ml 1% PTA solution with 70 ml absolute ethanol. Finally, the sample is washed in 70% ethanol. [2]

2.2 Approaches of mouse brain imaging with µCT

Embryonic mouse brain imagining with micro-CT was introduced by ORHAN et al. [34]. The approach from the article will be briefly explained. Firstly, the brain is extracted and placed into 10% buffered formalin followed by soaking in Hypaque diluted 1:10 with PBS. Next, the brain is transferred in micro-CT into a sample holder sealed with a plastic film to prevent dehydration. The location and number of axial images are set to cover the whole brain area. The voltage of 45 kV and a current of 177 µA is used for scanning. One thousand projections are taken with an exposition time equal to 300 ms. The total acquisition takes 5 hours, and the final voxel size is 16 µm. [34]

Another approach of mouse brain imagining is described below from [51]. The brain is not removed, but the segmentation algorithm is applied to subtract the demanded section from a 3D CT scan of the entire mouse embryo. The phosphotungstic acid (PTA) is used as a contrast agent for staining to enhance the contrast. A stained brain is placed into a polypropylene tube and filled with agarose to prevent movement while scanning. The micro-CT scanning is done using these parameters: 2200 projections with an exposure time of 900ms, voltage and current are 60 kV and 200 µA, respectively. The final voxel size is 5 µm. Finally, the tomographic reconstruction is done, and the brain area is manually segmented using software VG Studio MAX 2.2 (Volume Graphics GmbH, Germany). [31] [51] [34]

2.3 Comparison of µCT with medical CT

There is no fundamental distinction between µCT and medical CT. The X-ray source detector gantry spins around the item and takes 2D radiographs from numerous angles ranging from 0° to 180° or 360° while performing a scan with a medical CT. The sample rotates from 0° to 180° or 360° around its axis in most µCT systems, while the X-ray source and detector remain stationary at a fixed distance apart. The most significant advantage of using µCT, and a difference from medical CT, is the resolution which can go down to 1 µm by decreasing the voxel size. However, a higher X-ray radiation dose and longer scan time are needed to achieve a high-resolution image and improve the signal-to-noise ratio. [54]

3   Segmentation of Choroid Plexus

This chapter focuses on the localisation and segmentation of choroid plexus within micro-CT imaging data of an embryonic mouse brain. The segmentation aims to identify and label a specific area within an image. Thus the segmented image has multiple regions which are disjunctive among each other. The regions are marked either by colour or numbers to be distinguished. [19]

The segmentation methods can be subdivided into various groups:

Segmentation based on homogeneity

It is a pixel oriented approach. The homogeneity within an area is defined as a constant value with some tolerance of a chosen parameter. The parameter can be a scalar (intensity) or a vector. The basic method within this group is thresholding. However, the noise can cause a problem as the image will not be labelled as homogeneous. Thus there is a limitation in the use of this approach. [19]

Regionally oriented segmentation

This method uses specific local parameters to describe an area. Thus it is very similar to the previous approach. The example is a region growing algorithm. First, the initial pixel is chosen (seed), and its neighbourhood pixels are investigated by examining their values with some criteria. Then, the suitable pixels are added. [19]

Edge-oriented segmentation

Rapid intensity changes of pixels can point out the edge presence. Firstly, a parametric image is computed, which inducts the edge locations. Then, the obtained image with detected edges needs to be improved to have slim curves describing object borders. The final segmented image is determined from edge representation using a particular method. [19]

Flexible and active contours

This method is based on predefined object boundaries (e.g. manually). Then, an optimisation process is applied to maximise the fitting and adjust the position of the edges. [19]

3.1 Proposed methods for Choroid Plexus Segmentation

The most known method, also considered the gold standard, is manual segmentation. However, this approach is very time-consuming. Thus possible segmentation improvements used for segmentation are listed in this chapter. These methods are utilized for choroid plexus segmentation from µCT data data. The desired output from the segmentation is shown in the figure 3.1. [49]
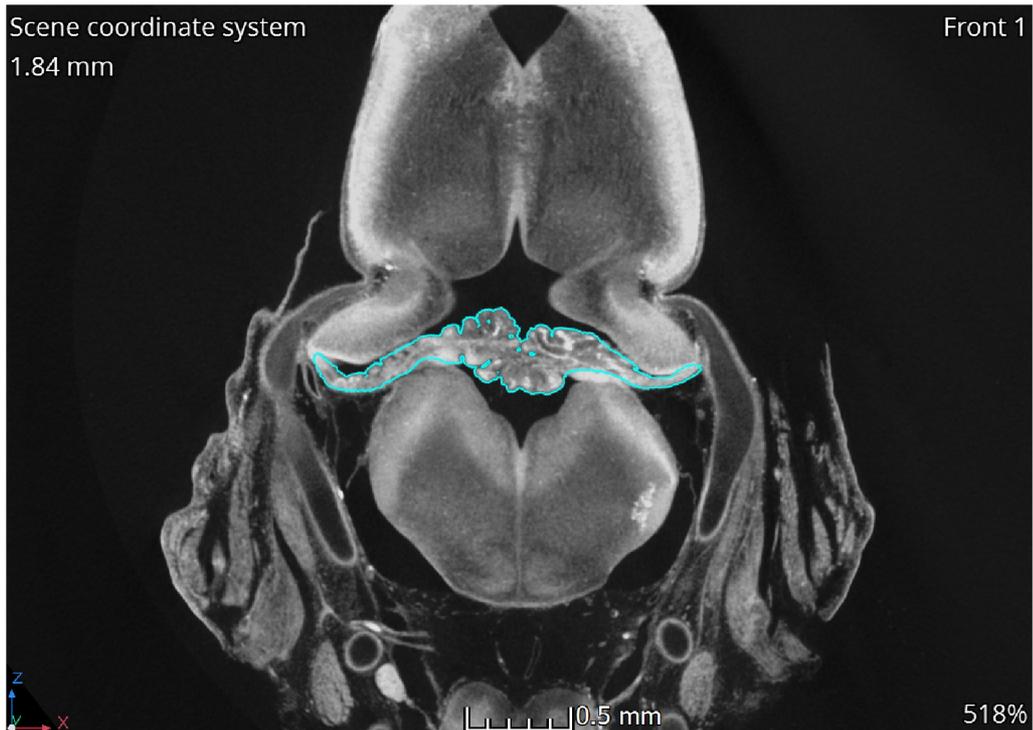
Fig. 3.1: Example of segmented region of choroid plexus in CT data of mouse embryo. The segmented region is within a blue line.

3.1.1 Gaussian Mixture Model Segmentation of Choroid Plexus in lateral ventricles

The first possible ChP segmentation process is to use an algorithm based on Gaussian Mixture Model (GMM), which is very well known in machine learning. The study describing the segmentation of choroid plexus using GMM on µCT data has not been introduced yet. Therefore, a method developed on T1-weighted MRI data will be demonstrated. Two independent datasets were obtained, the first enhanced with contrast and the second with no contrast. The results were compared with

manual and automated segmentation obtained by Freesurfer (software for image processing). [49]

Manual segmentation

Manual segmentation was done by two researchers using ITK-SNAP (version 3.8). First, the ChP in the lateral ventricles was segmented within the T1-w MRIs. The researchers' outputs were then combined to get one map for MRIs enhanced with contrast and one without contrast. [49]

Automatic segmentation

Automated segmentation was done in Freesurfer, which uses a probabilistic atlas for segmentation. The atlas is created using manually labelled data. Then, for each label for each voxel, the atlas provides the likelihood of each label given the category of nearby voxels and the probability distribution function of voxel intensities. Normalizing the new subject to the common space and adding the subject-specific voxel intensities to determine the ideal segmentation that optimizes the likelihood of observing the input data is how a new image is segmented. [49]

Gaussian Mixture Model

GMM is often used in image segmentation and is an unsupervised machine learning method. Thus, the labelled data are not required. The voxel intensity is represented by the finite number of Gaussian distributions. The number equals the number of groups, and each distribution describes one class. The distribution is characterized by mean and variance. The task is to optimize these parameters to find the distribution that fits the data the most using the Expectation-Maximization (EM) algorithm. The GMM was used to distinguish CSF, ventricular wall, and ChP voxels. [49]

Firstly, an algorithm generating a mask of lateral ventricular was used (Freesurfer), followed by applying GMM with two groups on masked voxels. Then, voxels were grouped into two groups depending on the average intensity which is either low or high. The ChP and lateral ventricular wall voxels were included within the group with a higher average voxel intensity. Next, the higher average voxel intensities cluster was smoothened. This step uses the fact that ventricular wall voxels are smoothed with surrounding CSF voxels (CSF voxel value within the mask = 0), resulting in a lower intensity value after smoothing. In contrast, ChP voxels are smoothed with nearby ChP voxels (ChP voxel value within the mask = 1), resulting in a higher intensity value after smoothing. Finally, the second GMM with three

components is applied, and the voxels belonging to the class with the highest mean intensity were chosen as final ChP voxels. [49]

Results

The outputs from GMM, manual and automatic segmentation using T1-w MR1s were compared. The GMM performance is more promising than automatic segmentation by Freesufer software and is comparable to manual segmentation. Furthermore, the average dice coefficient between segmented models obtained from manual and GMM segmentation is higher than between the manual and Freesurfer segmentation. Thus the GMM remarkably improved automatic segmentation. [49]

3.1.2 Choroid Plexus Segmentation using optimized 3D U-NET

The segmentation of the choroid plexus can be performed using deep convolutional neural networks, which are very successful if the field of medical image processing. 3D U-Net was optimized for the plexus segmentation in images acquired from magnetic resonance (MR). First, the ground truth was obtained with FreeSurfer, where the normalization and skull stripping is done initially, followed by the brain parcellations pipeline. Next, the outputs from the FreeSurfer were manually corrected and used as a ground truth. The U-Net model was optimized by replacing the activation function with the parametric rectified linear unit (PReLU), providing more parameters to adjust the activation level. Another optimization was done by including more features (96) at the first level of convolution as it is typically used. Two 3x3x3 kernels were used on every convolutional layer. Batch normalization, activation, and a 2x2x2 max-pooling layer were added after the convolutional features. The encoding and decoding levels were three layers deep. A 0.5 dropout rate was employed at the bottom layer. Patches were randomly chosen from training subjects with strides of 1x1x1. The patch size was chosen carefully to minimize the label imbalance within or between patches. The small patch size would reduce the imbalance in patches, but many patches won't have plexus regions. The intra-patch label imbalance was reduced using the bigger patch size. But again, most of the patches did not contain the plexus region. The patches were retrieved based on the probability that a patch with more choroid plexus pixels is more likely to be chosen for training to deal with the inter-patch imbalance. A weighted binary cross-entropy loss function was utilized to handle the intra-patch imbalance. The weights of the choroid plexus and background regions were 0.9 and 0.1, respectively. [55]

Results

The 3D U-Net showed satisfying results for the segmentation of the choroid plexus and is an efficient tool to measure the plexus quantitatively. The method showed higher accuracy in the sensitivity and dice scores than the atlas-based segmentation by the FreeSurfer. Furthermore, the number of features could be further tuned for each patch size to attain the optimum performance. Fourth, other loss functions could be investigated for improved performance. [55]

3.1.3 Choroid Plexus Segmentation based on a Region Descriptor

Machine learning techniques were used to segment choroid plexus in ultrasound images automatically. The method was based on a region descriptor that represents the local intensity and shape of the structure without explicit models. The segmentation was done in two steps. The candidate region was selected in the first part. Secondly, the region-based descriptor combined with a boosting classifier trained to recognize the wanted area was used for the region characterization. Thus the features describing the region were extracted, followed by classifying the areas by a trained classifier based on these features. First, the candidate region was selected by identifying maximally stable extremal regions (MSERs) within the image. Next, features were extracted from MSERs to form a region descriptor. The choroid plexus regions had to be identified among the MSERs. A rich region-based feature descriptor was constructed to determine the wanted region. The regions were distinguished by their shapes. The region's shape was compared with the templates creating a first shape descriptor. The second shape descriptor was based on a polar-histogram describing the area distribution centred on the region centroid and providing 60 features. Furthermore, six more features were extracted from intensity, scale and location information: mean intensity, histogram of pixel intensities in the regions, length of the minor and major axes of the region, the eccentricity of the region, X and Y coordinates of the region centroid, and histograms of the normalized X and Y components of the region pixel coordinates. In total, the region-based descriptor had 190 terms. Finally, multiple classifiers were compared for choroid plexus classification: AdaBoost, RUSBoost, and support vector machines. [17]

Results

The segmentation of multiple brain structures can be accessed with the region-based descriptor. There is no need for particular settings for a different structure. Thus the method is generalizable to other brain structures. Furthermore, the method is

fully automatic and works well on clinical data. RUSBoost classifier showed the best results for identifying the choroid plexus among multiple MSERs. [17]

3.1.4 Active contours

Active contours were used to segment the cerebrospinal fluid in brain CT images [36] [6]. The method uses an initial mask to define a region of interest. The shape of this mask is changed based on information from the image. It is based on the minimalization of the energy associated with the current mask/contour. There is external energy defining information in the image and internal, which considers the shape of the contour. Internal energy controls the contour's smoothness while the external force attracts the shape towards the region of interest. Active contours can be divided into edge-based models (geodesic active contour model) and region-based models (active contour without edge (CV)). The edge-based model uses a gradient to define. However, the method is not working correctly on data where the boundaries are not defined by gradient where the contour may pass through the edge. Instead, CV determines the object border by looking for locations with a uniform intensity distribution. This method achieves better results in the segmentation images with noise and weak object boundaries. The new approach was introduced by implementing a region-based active contour model, which is not sensitive to the initial contour, noise and intensity inhomogeneity. A range domain kernel function was incorporated into this model and is included in the range weighted function, resulting in automatic boundaries detection. The weights for pixels within the detected boundary region are increased. Therefore, the active contour is attracted to the boundary, and the method is insensitive to the initial contour. The problem with the intensity inhomogeneity is overcome by using a space domain Gaussian kernel function. An edge indicator function is added to the total variation to enhance results. [36] [6]

Active contours were also used for the choroid plexus segmentation. The starting point was chosen manually in the cavum septum pellucidum, overlapping with the choroid plexus. The outline was specified using a level-set function. The geometric term was included in a minimalization of the cost function as there is a geometrical prior to the location of the choroid plexus by choosing the seed point. Firstly, the ventricles and cavum septum pellucidum were segmented. Next, the choroid plexus was segmented, where the geometric term was used to constrain the segmentation of being close to the segmented region from the first step. This criterion was applied mainly in the frontal area, where the plexus does not have distant extensions. The distance map was computed to implement the constraint of being away from a region.[41]

Results

Active contours models achieve great segmentation results, and this new approach of region-based active contour model [36] is insensitive to starting contours and robust to intensity inhomogeneity and picture noise. Furthermore, the experimental findings showed that the proposed method could produce segmentation results with high accuracy compared to standard models.

3.1.5   Ventricle Segmentation

The localization of the choroid plexus can make a segmentation procedure more straightforward. The knowledge about its anatomical localization within the embryonic brain can be used. Therefore the segmentation of the fourth ventricle, where the plexus is located, can precede the plexus segmentation. [16] [4] As the first example, the method described by QIAN et al. ([37]) will be briefly explained. The segmentation of the ventricle was done on brain CT images. The goal was to use anatomical knowledge. Once the images were aligned, the segmentation of the ventricular region was done by taking the largest three-dimensional connected component of the low-intensity category. [37]

Another possible method for ventricle segmentation was proposed by Liu et al. ([29]). The segmentation was again done on CT images. The segmentation was done in a few steps. Firstly, a predetermined volumetric model was registered into the image, followed by further analysis of this registered model by determining eight regions of interest (ROI). Next, the cerebrospinal fluid was segmented by assigning its threshold within the ROI, allowing the cerebrospinal fluid segmentation from the entire brain volume. Next, each ventricle was segmented within its specified ROI. Finally, the segmentation was purified by identifying the intraventricular calcification regions. [29]

Chen et al. ([9]) did another ventricular segmentation by combining low-level segmentation and high-level template matching on CT data. First, the CT images were aligned with skull symmetry and anatomical features. Then a low-level segmentation was applied to each pixel as the ventricle region has a darker colour than the surrounding tissue. However, the binary thresholding, which could be used for the low-level segmentation, showed poor results caused by noise and blurry or even missing boundaries between different structures. So instead, the conditional probability models were applied. The models choose the most probable label of a pixel by analyzing features of both the pixel itself and its surrounding pixels. Maximum A Posteriori Spatial Probability (MASP) and Iterated Conditional Modes (ICM) were evaluated. The initial assumptions were made for both methods by assuming that every pixel has features representing its label and grey-level intensity creating

two new images, L and G (L contains the labels and G grey-level values for each pixel). The model implies that the labels generate each image's grey scales through some technique. Next, a 4-neighbourhood or 8-neighbourhood is analyzed around each pixel. Two assumptions are made within each pixel's neighbourhood. First, the grey-level value of the pixel leans just on its label. Second, the dependence between the labels is local. Local dependence is treated differently by ICM and MASP. A template matching algorithm follows the low-level segmentation to identify the segmented object as ventricles. First, non-ventricle areas are segmented, and size and position limits are applied. Then, more accurate exclusions based on location were achieved by mapping the template to the segmented image. The template was developed based on the annotated datasets from the Digital Anatomist Interactive Atlas of the University of Washington. [9]

Results

The ventricle segmentation showed promising results for all introduced approaches.A method proposed by Lui et al. showed optimistic results with noisy images and size variations of the ventricular system [29]. The second method introduced by Chen et al. improved ventricle segmentation by utilising anatomical features and spatial templates emanated from Magnetic Resonance data [9]. However, both models required prior knowledge of the ventricle model or its template. Therefore, a method introduced by QIAN et al. can be prefered in many scenarios where the prior knowledge about the structure is missing [37].

3.1.6 Segmentation of CT images using the concept of region growing

Another well-known method for image segmentation is a region growing algorithm. This approach was described and implemented for brain segmentation from CT data. The study focuses also on ventricles segmentation. The aim was to distinguish cerebrospinal fluid and tissue areas using a region growing and nearest neighbour classification algorithm based on predefined anatomic information. Segmentation can categorise the pixels into two classes of CSF and tissue by the mean intensities within these classes. A big part of the image is often affected by an inadequate signal-to-noise ratio or a cupping effect caused by a beam hardening, leading to intensity increase between high and low-density regions, resulting in incorrect pixel classification. Thus, it is essential to use another feature to segment the image accurately and implement image preprocessing to reduce artefacts before the segmentation. It helps setting thresholds between different brain structures by analysing the image histogram. The study selected the bivariate spline function

to eliminate the cupping artefact during the image preprocessing, followed by the intensity-based pixel classification. The research is based on the fact that particular pixels in a brain scan may be easily categorised as tissue or fluid with a high degree of certainty. Firstly, the pixels far from the fluid and tissue intensity distributions overlap are thresholded. Then, the rest of the pixels are classified by analysing their neighbourhood to perform more precise segmentation. [39]

The segmentation algorithm extracts the brain region by determining the skull edges followed by the 'seed pixel' identification for each class using their intensity values from the histogram and classifying the remaining pixels at last. [39]

The peak values within the histogram are selected as thresholds for direct pixel classification. The seed is chosen from the histogram area, which is below than the standard deviation of each group, by analysing the pixel intensity distribution. The seed is selected in the distribution part with no overlap with another group to represent its label best. In the region growing algorithm, the seed serves as a start point. In each iteration, the candidate's neighbourhood is analysed. Finally, the candidate is appended if the pixel neighbourhood satisfies the criteria, and this pixel is becoming a new candidate. [39]

Results

The thresholding segmentation does not produce acceptable results when used alone, as different groups' intensity distributions can be overlapped. Despite the constraints imposed on precision and accuracy by the partial voluming effect, the proposed algorithm is a valuable tool for segmentation. [39]

3.2   Comparison of Methods

Manual segmentation is the most straightforward approach considered the gold standard, although time-consuming. Another possibility is to use the neural network methods, which are unsuitable for analysis where the dataset is too small for the network's training. Furthermore, the GMM segmentation improved the automatic segmentation done by Freesurfer, which utilises a probabilistic atlas. The segmentation of the choroid plexus can be done by a region-based descriptor followed by a classification of the structures. This method showed massive potential in the segmentation of multiply types of brain structures. Active contours also showed successful segmentation results, although the disadvantage of this method is a need for manual selection of the initial seed point. Furthermore, the localisation of the choroid plexus can be accessed through ventricle segmentation which was also described. Finally, the model guided and template matching approaches can achieve

good segmentation results, but there is a need for preliminary knowledge of the model. Lastly, the region growing algorithm was described to segment brain structures within the CT data. It can be implemented for ventricle segmentation, but there is a need to choose the coordinates of the initial seed.

4 Segmentation of mouse embryo Choroid Plexus

This chapter describes the proposed approach for ChP segmentation within micro-CT data by introducing the data and detailed steps used to obtain segmented volume from the 3D imaging micro-CT data.

4.1 Data

Tab. 4.1: Samples of available mouse embryos. (WT - wild type, Mut - mutant)

Sample	Days post-fertilization	Type
Cdk13 sample 1	13	WT
Cdk13 sample 2	13	WT
Cdk13 sample 3	13	Mut
Cdk13 sample 4	13	Mut
Cdk13 sample 5	15	WT
Cdk13 sample 6	15	Mut
Tmem 107 sample 1	15	WT
Tmem 107 sample 2	15	Mut
Tmem 107 sample 3	15	WT
Tmem 107 sample 4	15	WT
Tmem 107 sample 5	15	WT
Tmem 107 sample 6	15	Mut
Tmem 107 sample 7	15	Mut

The data used for the segmentation of choroid plexus are listed within the table 4.1. There are two types of models primary used for a gene mutations analysis, CDK13 and Tmem 107, respectively. The impact of complete loss of Cdk13 function during mammalian development has not been investigated. Therefore, the Cdk13 mutant (Mut) mouse model to explore a novel role of Cdk13 during mouse embryonic development was established. In the preliminary results, the mice with the mutated Cdk13 gene display distinctive morphological changes in ChP. Cdk13 genes play an essential role as master switches in cell cycle control [1]. A loss of function of the Tmem 107 gene will also be studied between the control wild-type (wt) mice and mutant. The gene showed strong enrichment in the tissue of the choroid plexus. In general, Tmem 107 plays a role in cilia formation and embryonic patterning [44] [43].

The samples were stained and scanned on micro-CT resulting in a 3D volume that can be used for image processing for further morphological or anatomical analysis. The CDK13 samples were scanned as a whole embryo, but only the heads were used for the CT scan of the Tmem 107 samples. Two types of samples have already been used in previous independent projects. Therefore there are scans of the entire embryos for one type and only heads for the second one. The samples are 13 and 15 days old post-fertilisation, and a gene-knockout technique obtains wild types and mutants. The choroid plexus starts to be visible in the 11th-day post-fertilisation. Thus, it is detectable within the micro-CT data of each sample, and its morphology differs among them.

4.2   Staining

Animal morphology research requires accurate visualization of three-dimensional structures for comparative, functional, and developmental studies. Yet, there are few generally applicable technologies for non-destructive whole-volume imaging of animal tissues. X-ray microtomography is an ideal method to obtain volumes of small biological samples but has a contrast limitation for non-mineralized tissues. Embryonic samples are primarily composed of soft un-mineralized tissue, which has a low contrast in CT imaging. Therefore, the staining of the samples have to be done to enhance the contrast in CT scans. The staining method does not affect the morphology of the scanning samples. Before the micro-CT scan, the samples of mouse embryos were stained in phosphotungstic acid (PTA) to enhance the contrast of soft tissue using a method published by Metscher [32]. The staining protocol is robust and straightforward. PTA binds strongly to a variety of proteins and connective tissue. Together with electron-shell energies that match standard x-ray source emissions, this property suggested that it could be a suitable stain for X-ray imaging. The staining protocol is described in table 4.2. [32]

Tab. 4.2: Staining method published by Metscher [32]

Stock solution	Staining protokol
1% phosphotungstic acid in water	30 ml 1% PTA + 70 ml absolute ethanol are mixed to obtain 0.3% PTA in 70% ethanol
	Samples are placed to 70% ethanol
	Samples are kept in the solution overnight or longer

4.3 Imaging

After staining, the samples were placed into 1% agarose gel in 15 ml Falcon conical centrifuge tubes to prevent the motion during the scanning. Micro-CT measurement was performed using GE Phoenix v|tome|x L 240 (Waygate Technologies, Baker Hughes Digital Solutions GmbH) laboratory system equipped with a nano focus X-ray tube with maximum power of 180 kV/15 W and high contrast flat panel detector DXR250 with panel dimension of 2048 px × 2048 px and 200 µm × 200 µm pixel size. The measurements were acquired with the following settings: acceleration voltage 60 kV, X-ray tube current 200 µA, exposition time was 900 ms. The average volume size is 1400 x 1400 x 1500 pixels per sample with an average voxel size of 4 µm. Voxel size for different samples are listed in table 4.3. An example of CT scans and the 3D volume of the mouse embryo is shown in the figure 4.1. The tomographic reconstruction was realized by GE phoenix datos|x 2.0 software.
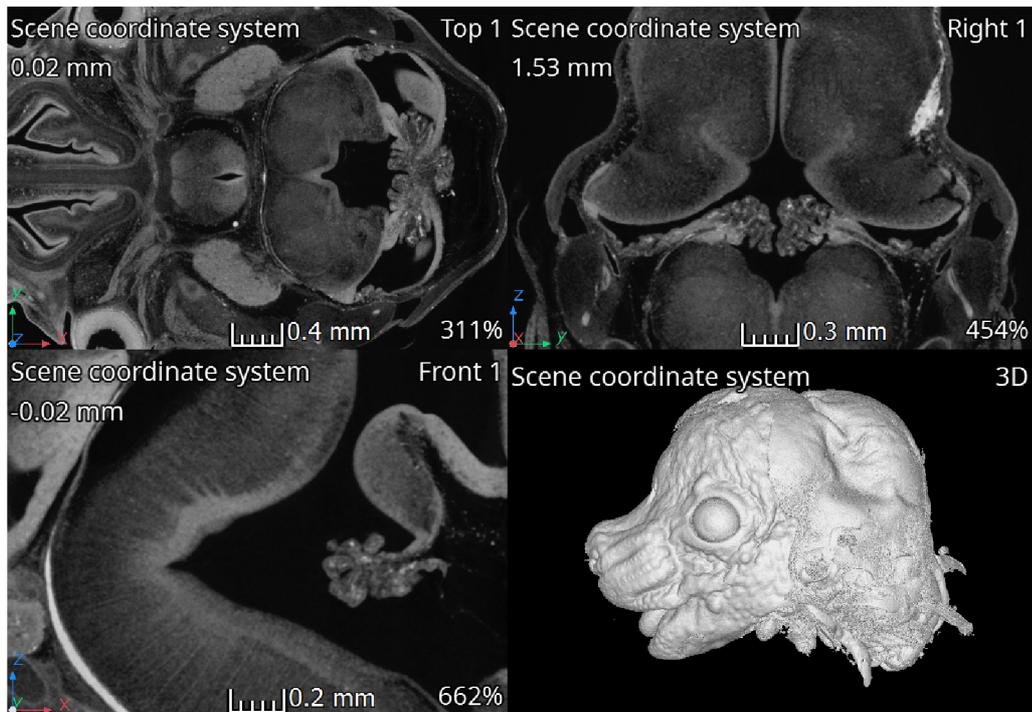
Fig. 4.1: CT data of mouse embryo. The choroid plexus is located within all of the chosen CT slices

Tab. 4.3: Voxel sizes of obtained sample volumes

Sample	Voxel Size [mm]
Cdk13 sample 1	0.0043
Cdk13 sample 2	0.0043
Cdk13 sample 3	0.0043
Cdk13 sample 4	0.0043
Cdk13 sample 5	0.0055
Cdk13 sample 6	0.0055
Tmem 107 sample 1	0.0045
Tmem 107sample 2	0.0045
Tmem 107 sample 3	0.0045
Tmem 107 sample 4	0.0032
Tmem 107 sample 5	0.0036
Tmem 107 sample 6	0.0036
Tmem 107 sample 7	0.0036

4.4   Segmentation

The segmentation of the choroid plexus was done for all samples, and the algorithm was implemented in MATLAB 2021. To obtain a precise model of choroid plexus, which will be further morphologically analyzed, the automatically segmented mask was imported to AVIZO 9.5 software (Thermo Fisher Scientific) to perform manual segmentation. This step was necessary as some regions were not included in a mask, especially the branches leading to the foramen of Luschka. The boundaries between the plexus and neighbouring tissue were not apparent at multiple locations resulting in artefacts which were also manually removed in AVIZO.

Multiple available approaches from researchers were analyzed and described in chapter 4, and a suitable ChP segmentation method was chosen based on their results. Any neural network segmentation approaches were not applicable as the size of the dataset is insufficient, and the structure of the choroid plexus is not consistent among samples. Furthermore, the segmentation method using GMM utilises masks of ventricle and choroid plexus created in Freesurfer using knowledge from labelled data. Thus this approach was unsuitable as the data set is not labelled.

Preprocessing

The image stack of CT volumetric data was loaded as a 3D matrix, and the segmentation of ChP was done in 3D. First, the matrix was converted into double format.

Consequently, the data preprocessing was done by histogram normalization among the samples. The histogram of the dataset is transformed to approximately match the histogram of the reference image, by using histogram-based intensity function and histogram equalization. One of the available samples was chosen to be a reference for the normalization of the entire dataset.

Segmentation of the 4th Ventricle

The choroid plexus is located in the fourth ventricle and runs along its inferior posterior wall [16]. Thus, the main idea behind the choroid plexus segmentation is firstly to segment out the ventricle area, which enables the plexus localisation in brain imaging data. Model-guided ventricle segmentation [29] and template matching [9] are methods designed for ventricle segmentation. QIAN et al. [37] introduced a simple method for ventricle segmentation in µCT data that does not require prior knowledge of the ventricle model or its template. The CSF recognition in CT images is based on its intensity, which is lower than for the other brain tissue [28] [15]. Thus thresholding is used to distinguish tissue from CSF. The proposed algorithm is described in figures 4.2 and 4.3. Firstly the volume is thresholded, using a threshold determined by the Otsu method, resulting in a tissue mask. Then, morphological closing is applied to mask to create a new mask which includes tissue and CSF. Next, the CSF is extracted by subtraction of tissue mask from the morphologically closed mask. Finally, the CSF regions are obtained, and the biggest connected region is chosen and labelled as ventricle.
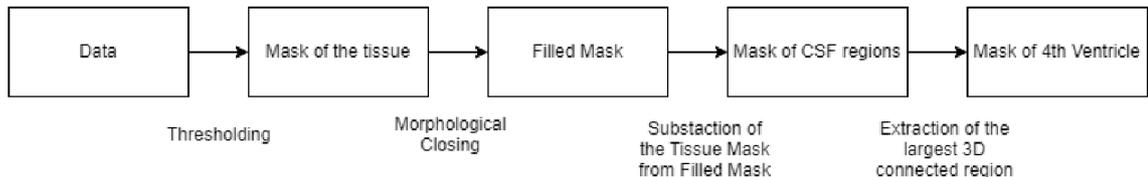
Fig. 4.2: Segmentation of the 4th ventricle using the image processing methods. The final region was obtained by extraction of the biggest 3D connected CSF region.
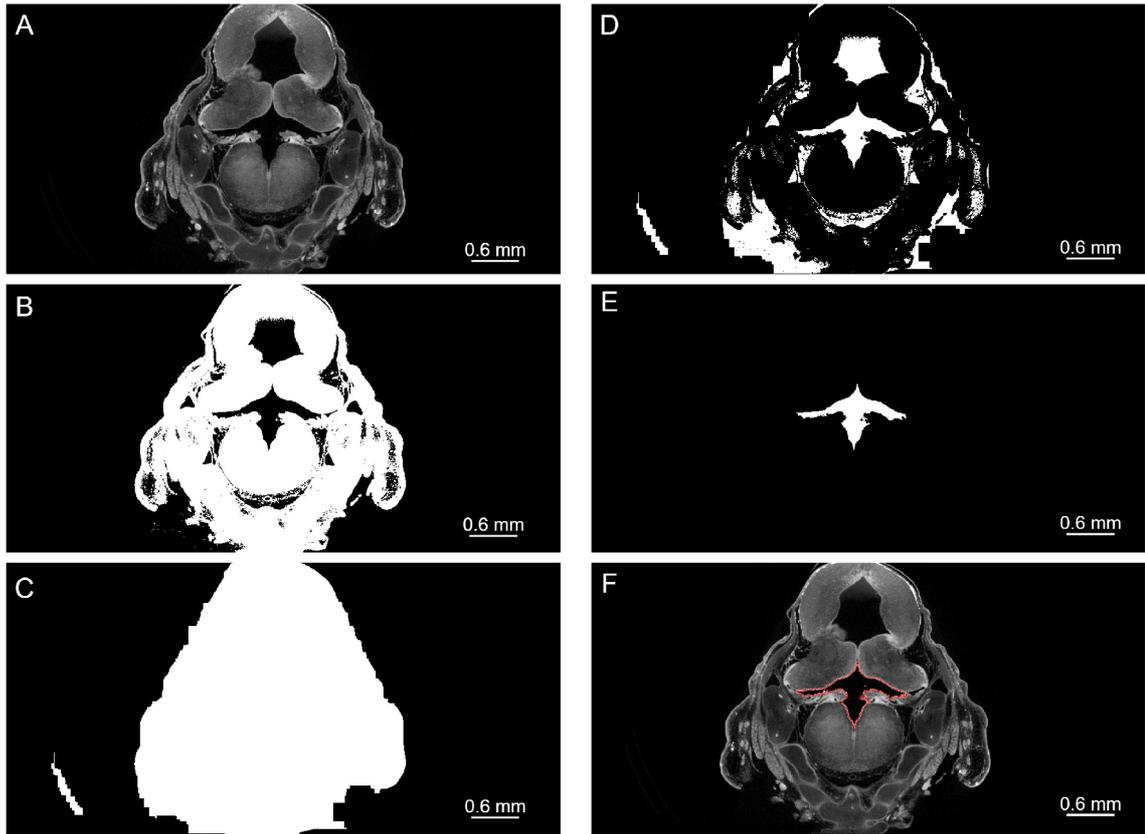
Fig. 4.3: The partial outputs of the fourth ventricle segmentation are presented through images a-f. (A) Mask of tissue obtained by thresholding; (B) Morphologically closed tissue mask; (C) CSF regions obtained by subtraction of the tissue mask from the mask obtained in (B); (D) Biggest 3D connected region was chosen to represent the fourth ventricle; (E),(F) final mask of the fourth ventricle. View: frontal plane. Sample: Tmem 107 sample 7.

Segmentation of Choroid Plexus

Firstly the data size was reduced by excluding slices which do not include ventricle. This step was necessary to save memory and shorten computational time. Then the top-hat filtering was applied, followed by a contrast enhancement to improve the intensity and enhance the edges. Contrast enhancement was done using a method which saturates the bottom 1% and the top 1% of all pixel values. This step was utilised to separate the objects with similar intensities on their borders. Top-hat filtering performs the morphological opening of the image and then subtracts the result from the original image [3].

Choroid plexus segmentation is based on its location within the ventricle [16] [4]. Therefore, the extracted mask of the ventricle was used. The mask included only the

regions with CSF and not the choroid plexus with a higher intensity than the liquid. The morphological closing was applied to the mask of the ventricle to include the plexus. Thresholding was used on the voxels within the masked regions to extract the choroid plexus from the ventricle. This approach segmented only a part of a plexus region. The areas that caused the limitation were the plexus is fully attached to the ventricular wall. So these voxels were not covered after the morphological closing of the ventricular mask. Therefore, the active contours (snakes) were used to add the remaining voxels to the final mask of the choroid plexus. The function to compute active contour is already implemented in MATLAB and uses the Chan-Vese method [6]. This method detects structures whose borders are not necessarily defined by the gradient, which is crucial as the plexus boundaries are not significantly apparent in many regions attached to the ventricular wall. The function has an input matrix of volume data, a primary mask of choroid plexus and the number of iterations. The number of iterations was empirically set to 100. The number of artefacts is increasing with a bigger number of iterations. The mask starts expanding above the ventricular boundaries. Then, the artefacts were removed by setting the voxels above the mask to zero. Removal was done in the coronal plane (thus in 2D), and only in the region above the mask, as in this area, the plexus is not connected with the ventricular wall. The artefacts within the region below the ventricular mask were removed manually in AVIZO. Artefacts located within both areas are shown in figure 4.4.

The segmentation of choroidal branches leading to the foramen of Luschka was challenging in multiple samples. These regions were poorly connected with the the medial choroid plexus within the centre of the fourth ventricle. These branches were manually segmented in AVIZO if required after the automatic segmentation in MATLAB. Automatically segmented masks were imported into AVIZO, where the segmentation was finalized by adding missing regions and artefacts correction, and the final volume was exported as the STL file. A figure 4.4 shows the regions manually added to the automatic segmentation. Finally, segmented masks were imported back to MATLAB.
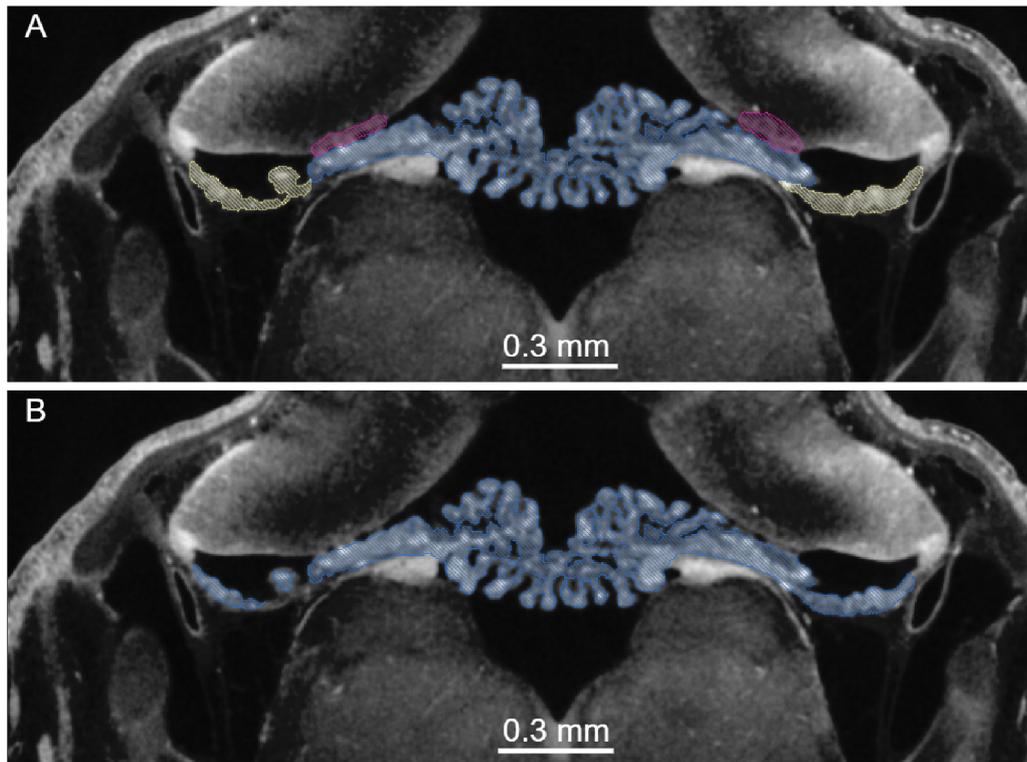
Fig. 4.4: Correction of segmentation. Blue region represents the choroid plexus. (A) Segmentation artefacts after the automatic segmentation: purple - artefacts created after the active contours approach was applied, yellow - parts of the choroid plexus, which were not included by automatic segmentation; (B) result of corrected segmentation where the purple artefacts were removed, and yellow regions, that were missing, were added to the final segmentation. (The manual segmentation was done in AVIZO)

5 Morphological Analysis of Choroid Plexus

The fourth ventricle's choroid plexus (ChP) is a tiny structure created by multiple villi arranged as a tight epithelium surrounding highly vascularized tufts, which hang from the tela choroidea inferiorly and swell into the cavity of the fourth ventricle. The L-shaped tufts extend into the foramen of Lushka creating Bochdakek's flower basket. Its role in cerebrospinal fluid production serves as an essential brain barrier. However, the morphology of the choroid plexus has been analyzed only in a few studies. [52] [22] [18] [35] Each brain ventricle produces ChP tissues, each with its own shape. The recent discovery of a correlation between ChP geometrical traits and human brain disorders has piqued interest in learning more about the morphology of this understudied area of the brain. Obtained models of segmented choroid plexus were morphologically analyzed. The methodology will be further explained in this chapter. All morphological analyses were done in MATLAB [52] [22] [18] [35].

5.1 Volume and Area

The first ChP analysis was focused on the determination of the volume and the area of the segmented model for each sample. Plexus volume may differ in population physiologically for some regions, such as Bochdalek's flower basket [35]. The volume was computed as the number of voxels in the areas within the volumetric binary image multiplied by the voxel size.

$$Volume = NumberOfVoxels * VoxelSize^3 \quad (mm^3) \qquad (5.1)$$

The volume was converted to a sphere radius of equal volume using the following equation

$$radius = \sqrt[3]{\frac{Volume * 3/4}{\pi}} \quad (mm) \qquad (5.2)$$

Crofton formula was used to efficiently determine the area of the binary model of the choroid plexus as the distance around the boundary of the region [26]. Usually, the edge of the 3D object is reconstructed using marching cubes, and then computation of the surface is done by summing the area of individual triangles. The Crofton method is based on counting the intercept number of the model edges with a group of isotropic test lines. The surface area S of the 3D object is then computed using the following approximation

$$S(X) \simeq 4 \sum_k \frac{c_k}{\lambda_k} \chi(X \cap L_k) \quad (mm^3)[26] \qquad (5.3)$$

where L_k is a group of 3D discrete lines parallel to direction k, c_k is the discretization weight associated with 3D direction k, and λ_k is the density of discrete lines in direction k.

The density of a line is calculated by dividing the distance between neighbouring voxels in direction k by the volume of a single voxel. Weight c_k is equal to 1/3 if the number of directions is 3. Otherwise, if the number of directions is bigger than three, the weight for each direction is equivalent to the relative surface area of each spherical domain by projecting each direction on the unit sphere. Intercept counts are calculated using run-length encoding. The run-length encoding collects all pixels on a single line into one element. When the binary object is small enough, run-length encoding reduces the number of components necessary to represent the item compared to a standard pixel representation. In addition, because of the run-length encoding, it is possible to compute the binary object's intercepts line by line rather than pixel by pixel. [26]

Finally, the obtained surface area was converted into a radius of the sphere of the equal surface using following equation

$$radius = \sqrt{\frac{S}{4 * \pi}} \quad (mm) \tag{5.4}$$

5.2 Growth Angle

The growing angle of the choroid plexus from the foramen of Magendie into the fourth ventricle has not been studied yet. Therefore, the angle was estimated between the direction vector of the choroid plexus and the frontal plane placed posteriorly to the fourth ventricle. The choroid plexus grows ventrally from the frontal plane into the ventricle. The computation was accomplished using the 3D model of the choroid plexus. Eigenvectors were utilized to calculate the orientation of the fitted ellipsoid that has the same normalized second central moments as the model of choroid plexus. The eigenvalues must be determined before the eigenvectors are computed using the following equation

$$|A - \lambda \cdot I| = 0 \tag{5.5}$$

where A is a matrix, λ is the eigenvalue, and I is the identity matrix. The eigenvalues are in descending order. Thus the first eigenvalue determines the biggest variability. Then, the eigenvectors are computed using the formula

$$A \cdot v_k = \lambda_k \cdot v_k \tag{5.6}$$

where v_k is the k-th eigenvector, and λ_k is the k-th eigenvalue. Finally, the angle is computed using the first eigenvector, which defines the direction of the model, and the vector of the frontal plane (Z-axis) which equal to $\vec{u} = \langle 0, 0, 1 \rangle$. The angle is then computed with following formula

$$angle = cos^{-1}(\frac{\vec{u} \cdot \vec{v_1}}{\|u\| \, \|v_1\|}) * \frac{180}{\pi} \quad (°)[33] \tag{5.7}$$

5.3   Landmarks and Generalized Procrustes Analysis

The differences in the shapes among the obtained 3D models of the choroid plexus were estimated by choosing a proper set of landmarks, which were further analyzed by generalized procrusted analysis. Firstly, a landmark can be described as a point of correspondence that matches among the samples either by its anatomical or mathematical location. The landmark is chosen for each model at the exact location so that the variety of the landmark position can be utilized for model comparison. Exactly six landmark points were manually selected from each of the models in 3D Slicer using the Markups module. The locations of the chosen landmarks are shown in figure 5.1. The landmarks were selected on both sides of the branches endings of LHS in the foramen of Luschka, pair of points were selected on the top of the region between the MHS and a RSS on both sides, and another two points were chosen at the bottom of this location. [47] [12]
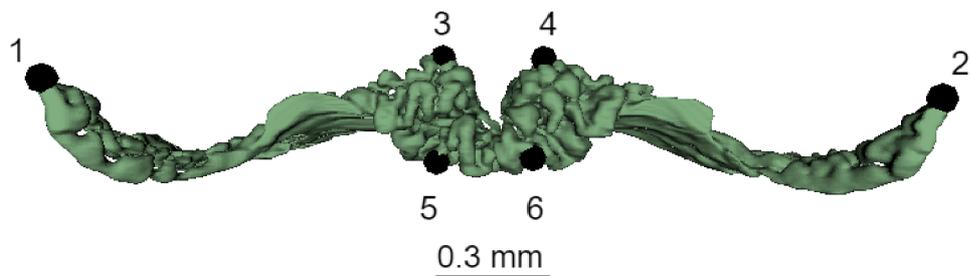
Fig. 5.1: 3D model of segmented choroid plexus with 6 landmarks. Frontal plane. Sample: Tmem 107 sample 1

Secondly, the generalized procrusted analysis (GPA) is computed to determine the variation among the models by comparing each model to the determined mean model. The GPA uses Procrustes distances, defined as the minimal distance between two points. This distance is minimalized by geometric transformation as scaling, rotation and translation [13]. The procrusted distance is computed from the geometrically aligned points as the sum of squared differences between sample points and mean shape points. So the GPA method provides the shape alignment where the effects of the translation, scale and rotation are filtered out. The GPA computation follows four steps: 1. The initial mean shape is estimated by choosing the first model; 2. The remaining shapes are aligned to the mean shape; 3. The estimate of the mean shape is re-calculated from the aligned shapes; 4. If there is a difference between the estimated mean shape and the initial means shape, the algorithm returns to the second step. So, the model converges to the solution when the shape is not significantly changing within the further iterations. Furthermore,

the estimate of the mean shape is computed using Procrustes mean:

$$\bar{x} = \frac{1}{N} \sum_{i=1}^{N} x_i [47]$$ (5.8)

where N is the number of models, and x_i is the i-th shape. The shape of each model is defined by the selected landmarks. Finally, landmarks are transformed using the derived mean model from the GPA, and the distances are computed as the sum of squared differences between the transformed landmarks and landmarks of the mean model. This computation is done for each sample with the mean model. [5] [10] [23] [47] [13]

Statistical evaluation of the Generalized Procrustes Analysis

Principal component analysis was performed to model shape variations.Principal component analysis (PCA) reduces dimensionality to enable the analysis of datasets with many features. The multidimensional space can be reduced into a few principal components, which will express a sufficient percentage of variability and show the main patterns of the dataset. The basic PCA computation will be further explained. [38]   [45] [21] Before the PCA is performed, the data are normalized by subtracting the average of each dimension $\bar{X}$ from each correspondent value X_i in $j - th$ dimension:

$$X_{ij}^* = X_{ij} - \bar{X}_j \quad [45]$$ (5.9)

Next, the covariance matrix is computed using the normalized dataset:

$$C = \frac{X^{*'} X^*}{n - 1} \quad [45]$$ (5.10)

where C is a matrix with n columns and n rows and, and n is number of dimensions.

The eigenvalues and eigenvectors are further calculated utilizing the covariance matrix. The eigenvalues show the variability for each dimension, and the eigenvectors indicate the directions of variability. [45] [21] The eigenvalues a and eigenvectors λ can be computed via covariance matrix C as:

$$Ca - \lambda a = 0 \Leftrightarrow Ca = \lambda a \quad [45]$$ (5.11)

Then, the eigenvectors are orders based on the eigenvalue in descending order. Thus the first eigenvector expresses the biggest variability within the dataset. Finally, multiplication with eigenvectors transforms the data into a space of principal components. [38] [45] [21] Thus, this method analyzed the aligned landmarks in 2D space by choosing the first two eigenvectors.

6 Results

Results of the choroid plexus segmentation and its morphological analyzes will be presented in this chapter.

6.1 Segmentation

The ChP segmentation was proceeded using the semiautomatic algorithm on 3D µCT data of mouse embryos. The implemented method uses the knowledge that the ChP is located within the 4th ventricle, so at first is done the segmentation, and consequently the extraction of ChP using thresholding (figure 6.1).
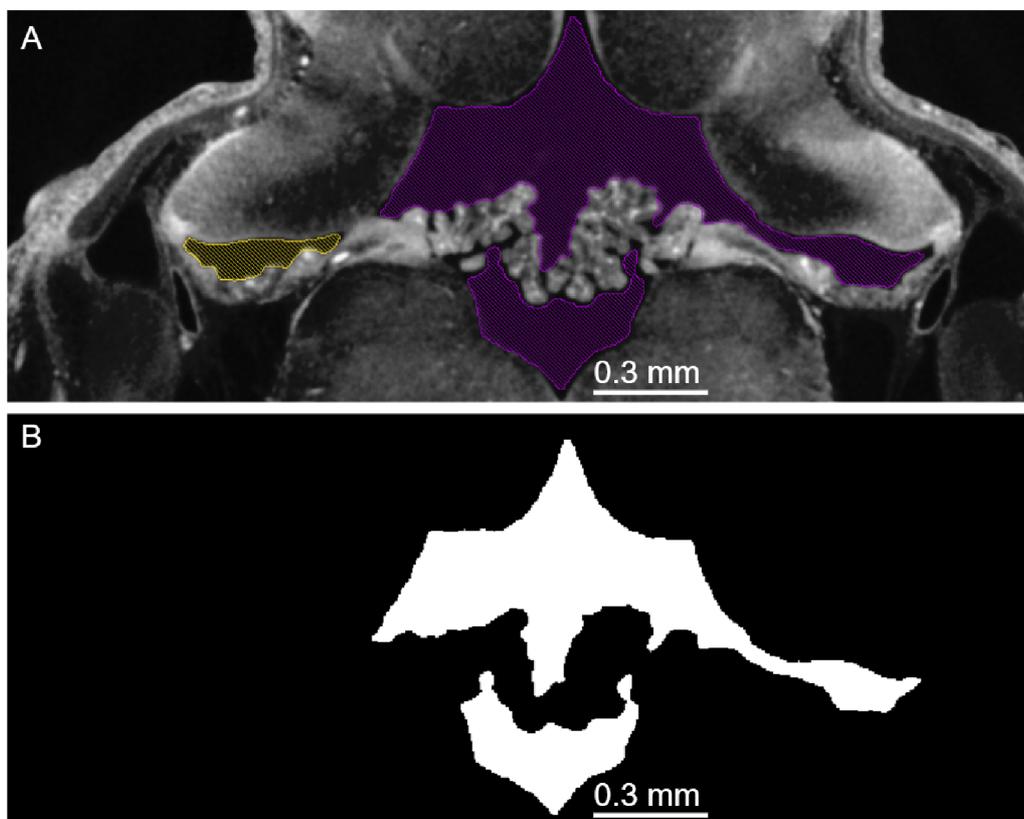
Fig. 6.1: Ventricle segmentation obtained after the biggest connected region was extracted from the area with low intensities representing the CSF within the brain. View: Frontal plane. The purple region the obtained segmentation and its mask is shown in (B). The yellow region belong to the 4th ventricle but was not included in the biggest connected region in this case. Sample: Tmem 107 sample 1.

Next, the active contours were applied to the extracted area to include all the choroidal parts. Finally, the artefacts were filtered out. Consequently, to obtain a

precise 3D surface model which can be further morphologically analyzed, the models were imported to AVIZO for manual segmentation of missing parts.

The extraction of the biggest connected region represented the area of the fourth ventricle. However, the choroid plexus extends into the foramen of Luschka, which connects the fourth ventricle to the cerebellopontine cistern. These parts are crucial for the segmentation of the choroid plexus and were not added within some samples, resulting in the missing segmentation of the lateral plexus lying in the foramen of Lushka. The example of the missing region of foramen of Lushka is shown in figure 6.1 (A) where the left foramen is missing in segmentation (yellow region). The missing plexus part was successfully added for some samples by applying the active contours model.
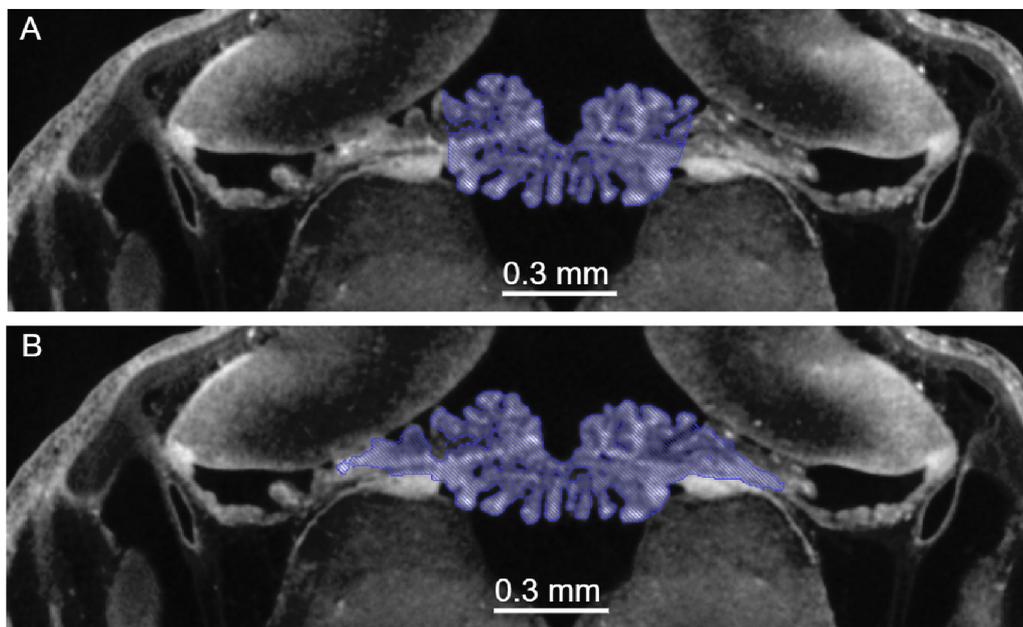
Fig. 6.2: The active contours model was applied to improve the initial segmentation (A) obtained after the thresholding of the ventricular region. The result is shown in (B). The number of iterations was chosen to be 100. Parts of the lateral ChP extending into the foramen of Luschka are still ignored. However, the number of artefacts formed outside the ventricular regions is minimal.

Figure 6.2 shows the segmentation results from initial segmentation compared with a results obtained after the active countours model was applied. Figure shows that the segmentation was not successful in the region where the plexus is attached to the ventricular wall. In these regions, the oversegmentation were formed after applying active contours. The number of artefacts was minimalized by a limited number of iterations used to perform the active contours method. The number

of artefacts increased with a bigger number of iterations, as shown in figure 6.3. Although, more missing regions of the choroid plexus were added with a higher number of iterations. Therefore, the number of iterations was set to 100, which proved the best accuracy of the segmentation.
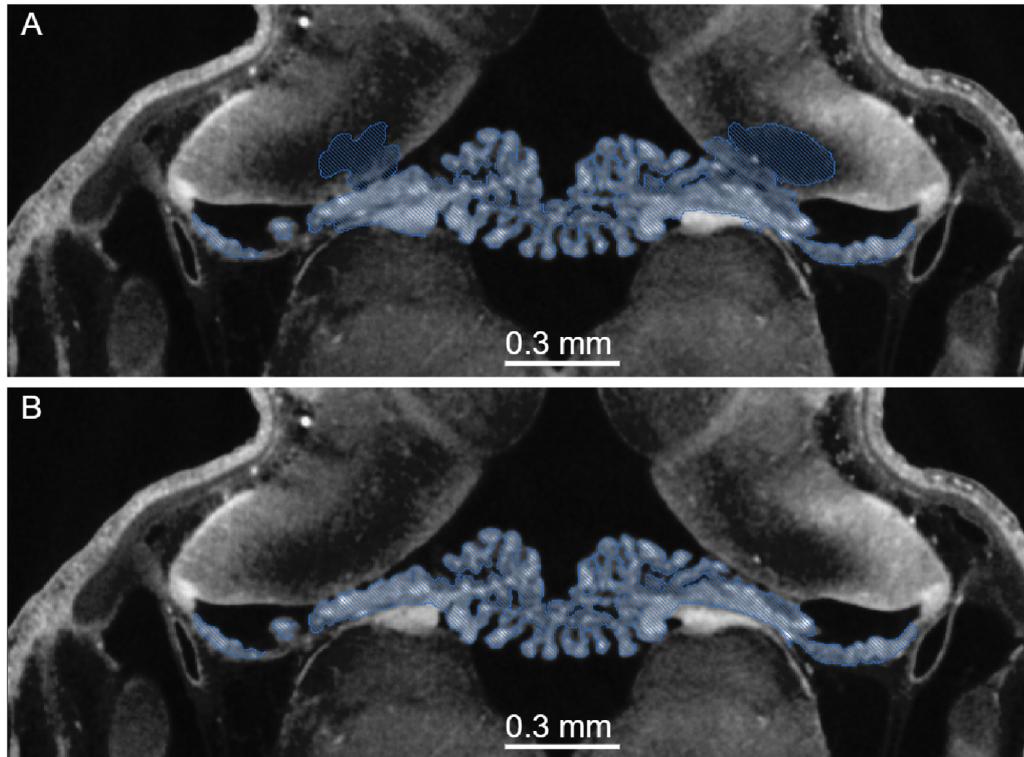
Fig. 6.3: An example of the artefacts formed by applying the active contours method with a number of iterations equal to 200. The entire area of the plexus is segmented, but the mask extends into regions outside of the ventricle. View: Frontal plane. Sample: Tmem 107 sample 1. (A) shows the oversegmented region where a high number of iteration caused a leakage outside of the ventricular region. A correct segmentation is shown in (B).

The artefacts produced by the choroidal mask elongation above the ventricular mask were removed by setting all the pixels located superiorly to the ventricular mask and set to zero. If there was a gap in the upper border of the mask caused by the plexus attaching the ventricular wall, the gap was filled by interpolating the closest values. Furthermore, the lateral plexus in the foramen of Luschka could have been affected by this filtering when the mask was not included in this area. Therefore, the mask was extended into both directions with the closest non zero value. The results are shown and described in figure 6.4.

In most cases, the lateral plexus in the foramen of Luschka has not been added

by automatic segmentation in MATLAB. The artefacts were caused by low contrast between the plexus and the surrounding tissue, added to the final volume by active contours.
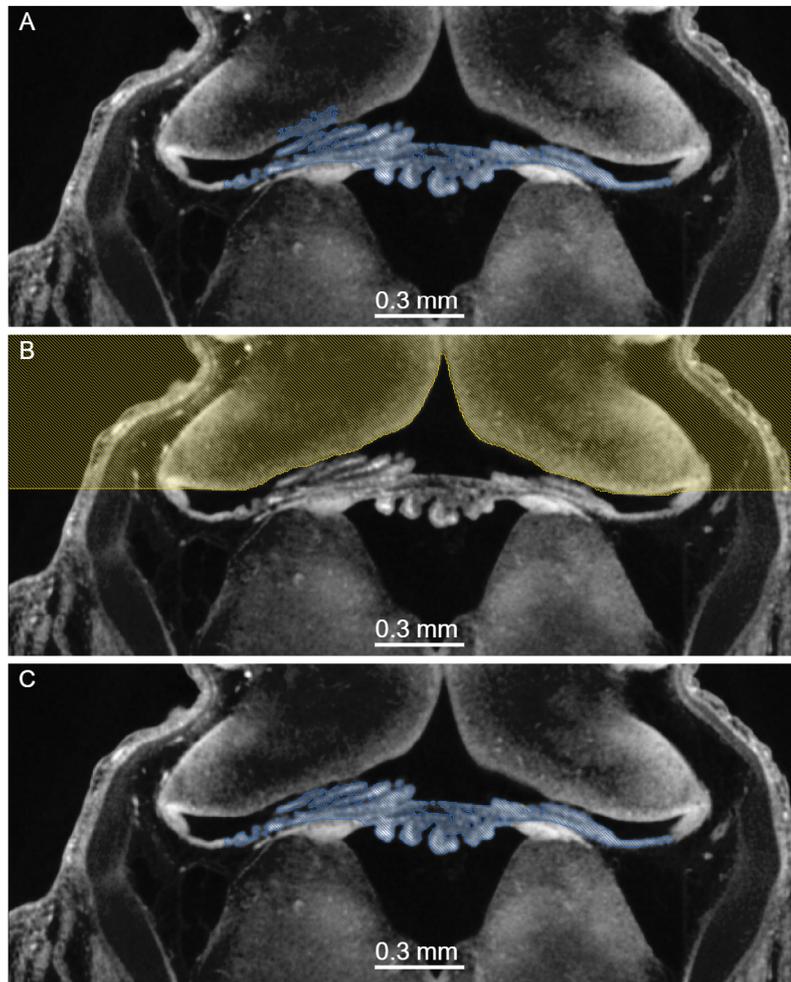
Fig. 6.4: Artefact formed outside the ventricular region is shown in (A). The mask was created by extracting the region above the ventricle in the frontal plane to remove the artefacts shown in (A). The mask was extended on both sides. The mask is shown in (B). (C) represents the result after the artefact removal.

The final volume of the choroid plexus is presented in figure 6.5, and the examples of the segmented area within multiple CT slices are shown in figure 6.6 to demonstrate the changing morphology of the plexus across the volume.

0.3 mm
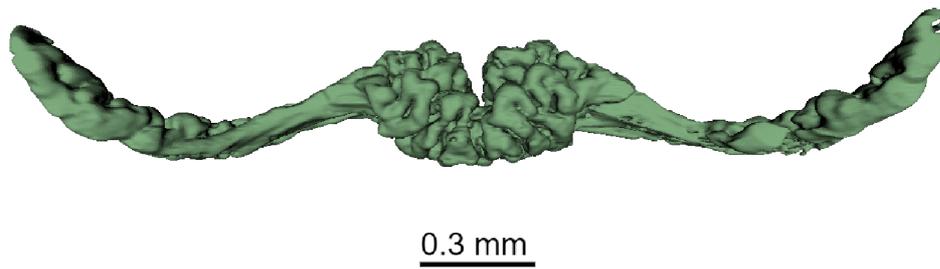
Fig. 6.5: Final 3D model of the segmented choroid plexus of the fourth ventricle. The model was manually corrected in AVIZO and exported as STL file. View: Frontal plane. Sample: Tmem 107 sample 1.
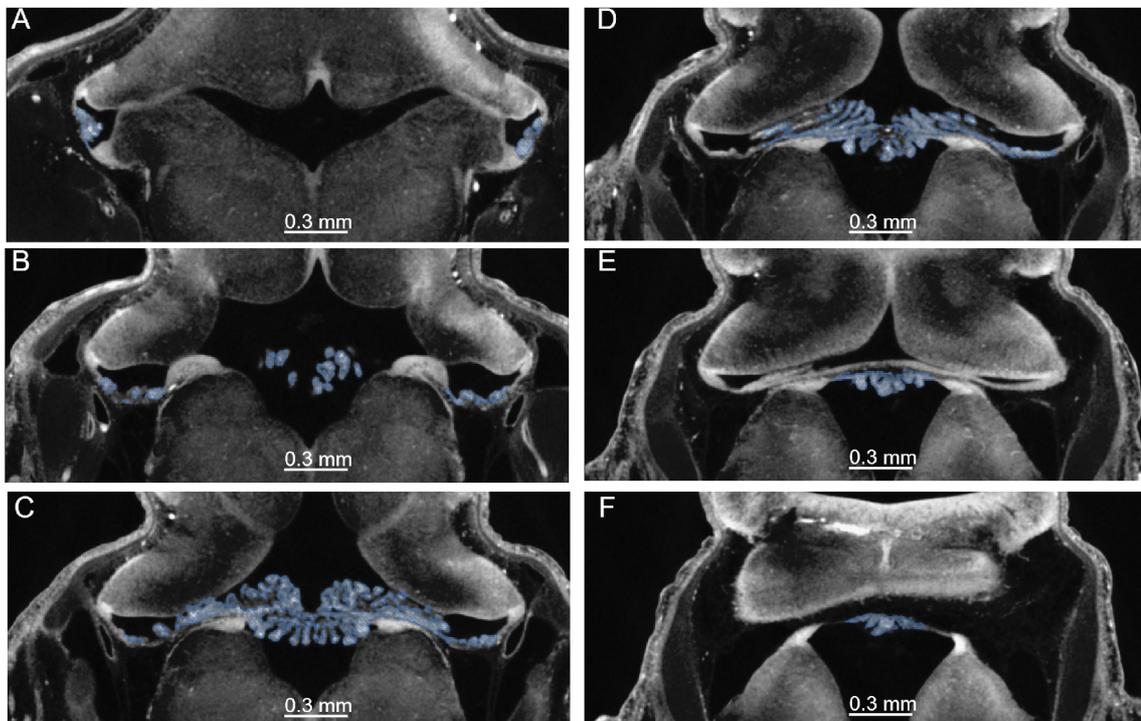
Fig. 6.6: Appearance of the choroid plexus on frontal CT scans at comparable levels. The segmented region of the choroid plexus is within the blue contour. Dorsal shift through a-f.

6.2 Morphological analysis

The morphology of the choroid plexus has been analyzed only in a few studies [52] [22]. However, the demand for knowledge about plexus morphology is increasing

caused of its discovered possible connection with multiple diseases. All 13 available samples were analyzed, and the results are summarized in this section. There are two groups of samples, Tmem and Cdk13. Both are formed of wild types and mutants. Cdk13 can be further divided into 13 and 15 days old embryos. The choroid plexus development begins around embryonic day 9.5 (E9.5) and peaks between E11 and E12 [30]. Therefore the 13 and 15 days old embryos were chosen to be analyzed. The goal is to implement a program that will provide a quantitative analysis of the segmented model and compare the samples to see if there can be a connection between the sample type and its features. Volume, surface area, growth angle and shape variations were investigated for each model of segmented choroid plexus. Firstly, the shape of the plexus was analyzed based on the [52] where the extension to the foramen of Luschka (known as Bochdalek's flower basket) and disconnection between the medial and lateral plexus was analyzed. The disconnection was not found in available data. Although, the missing extensions to the foramen of Luschka were seen in multiple samples. Furthermore, there were cases where the L-shaped plexus branches were not connected in RSS of the choroid plexus. The results are listed in table 6.1. Both of these observed abnormalities are shown in figure 6.7.

Tab. 6.1: Morphological aberrations. Only samples with at least one seen aberration are listed

Sample	Missing extension to the foramen of Luschka	Branches connected in RSS
Cdk13 sample 1	no	no
Cdk13 sample 2	yes	no
Cdk13 sample 3	yes	no
Cdk13 sample 4	yes	no
Cdk13 sample 6	yes	no
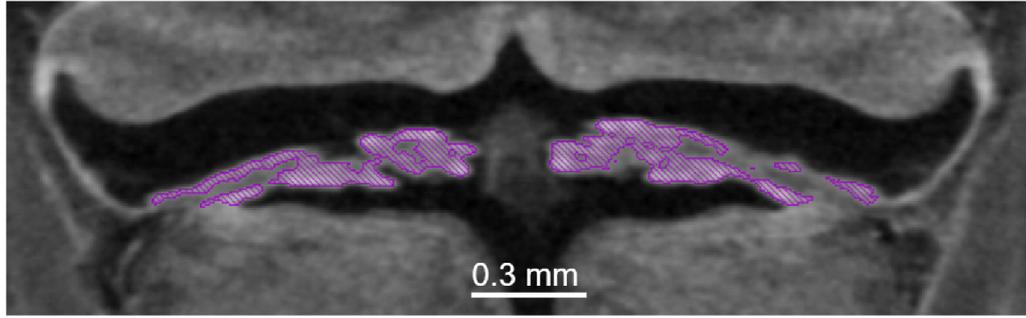
Fig. 6.7: Morphological abnormalities observed on Cdk13 sample 6

Volume and Surface Area

The first quantitative analysis was focused on determining the volume and surface area of each model. The volume and surface area have been already studied [22] [46].

Since the plexus morphology may differ within the population [22], it was not expected to obtain the same values for samples within the same group. The results are shown in table 6.2 for both volume and surface area. The values were converted into a sphere radius of equal volume (5.2) and surface (5.4), respectively. This step was done for expression of the differences between the samples. The radii are shown in figure 6.8.

Tab. 6.2: Volume and surface area calculated for each available sample.

Sample	Volume $[mm^3]$	Surface Area $[mm^2]$
Cdk13 sample 1 WT	0.0322	1.590
Cdk13 sample 2 WT	0.0180	0.904
Cdk13 sample 3 Mut	0.0117	0.648
Cdk13 sample 4 Mut	0.0042	0.343
Cdk13 sample 5 WT	0.0368	2.816
Cdk13 sample 6 Mut	0.0334	2.717
Tmem 107 sample 1 WT	0.0480	3.107
Tmem 107 sample 2 Mut	0.0393	2.522
Tmem 107 sample 3 WT	0.0380	2.454
Tmem 107 sample 4 WT	0.0473	2.967
Tmem 107 sample 5 WT	0.0545	3.062
Tmem 107 sample 6 Mut	0.0690	3.702
Tmem 107 sample 7 Mut	0.0403	3.475
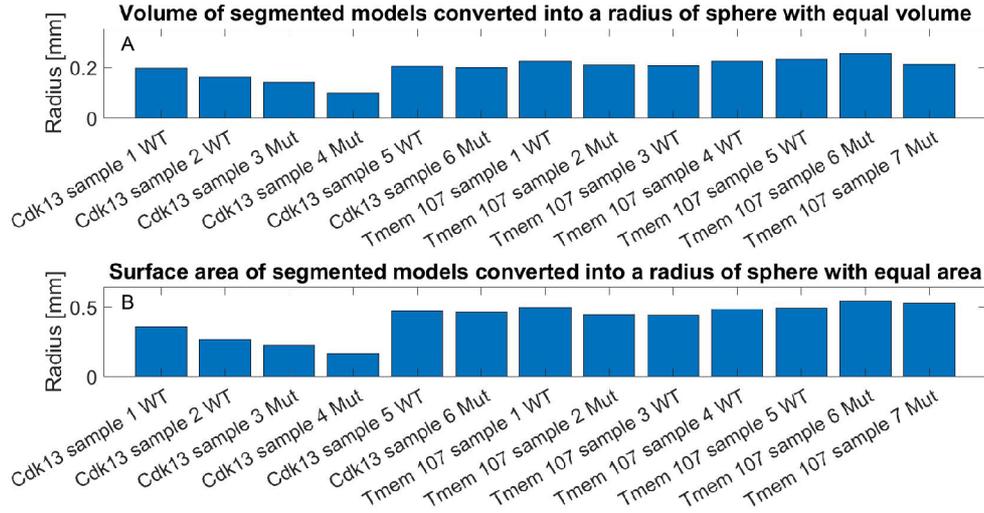
Fig. 6.8: Volume (A) and Surface area (B) of the all segmented models. Values were converted into a sphere radius with an equal volume and surface, respectively.

Figure 6.8 (A) shows the results of volume analysis. The corresponding radius demonstrates the resulting volume. The radius varies between 0.1066 mm and 0.2544 mm among all samples. Cdk13 sample 4 Mut was estimated to have the smallest radius among the 13 days old models and also among all the available models, equal to 0.1001 mm. On the other hand, Tmem 107 sample 6 Mut had the highest radius of 0.2544 mm among the entire dataset, not only within its group of 15 days old embryos. Furthermore, Cdk13 sample 5 WT had the smallest radius among the 15 days old models, 0.2063 mm.

The within-group volume differences were further analyzed by comparing the mean values. The results are shown in figure 6.9. Firstly the difference in radius between wild types and mutants from the group of Cdk13 E13 embryos was estimated by calculating the mean values of both types. The difference is equal to 0.0643 mm. Secondly, the 15 days old samples belonging to the Cdk13 group were compared. Only two samples are in this group, one wild type and one mutant. Therefore, the dissimilarity was computed by subtracting the mutant's radius from the wild type's, resulting in 0.0066 mm. Lastly, the difference between wild types and mutants of 15 days old Tmem 107 embryos was computed. The mean difference was estimated to be 0.0026 mm.
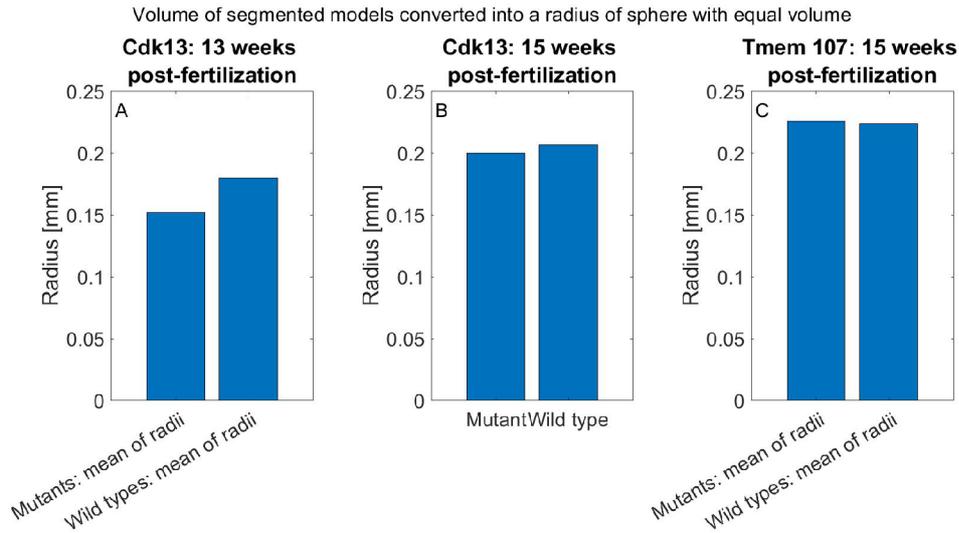
Fig. 6.9: Mean radius computed for mutants and wild types within the group of Cdk13, E13 (A) and E15 (B); The values were also computed for the group of Tmem 105 samples which are 15 days old (C).
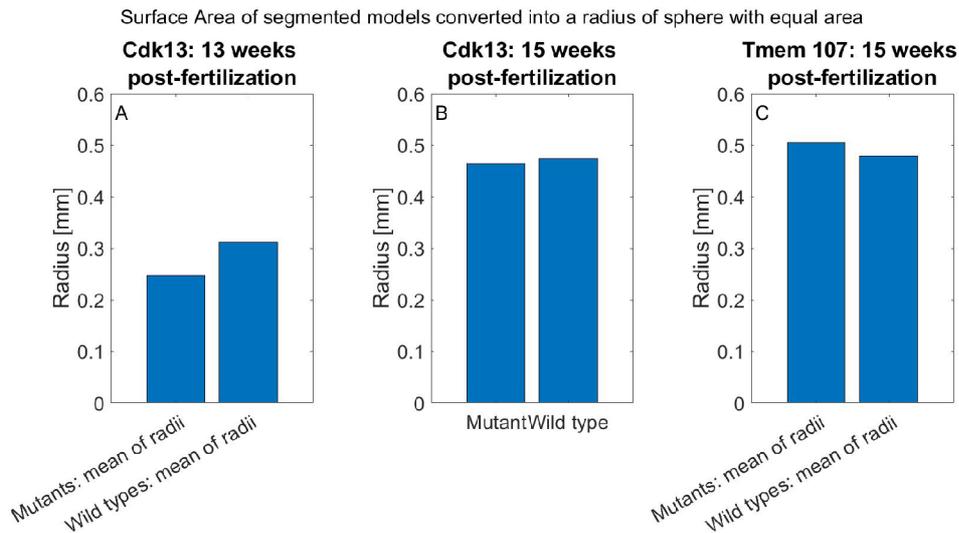
Fig. 6.10: Comparison of the mean radii between the wild type and mutant samples within the group E13 Cdk13 (A), E15 Cdk13 (B), and E15 Tmem 105 (C).

Furthermore, the surface area results are shown in figure 6.8 (B). The surface area was again converted into a sphere radius for better presentation. Comparing radii in figure 6.8 (A) and (B), it is possible to see the relationship between volume and surface area. The minimal and maximal radius samples are the same for the radii

computed from volume and surface area. Consequently, the high volume models also have high surface area values. The interval of radii calculated from the surface area is between 0.1652 mm and 0.5428 mm. The differences between the wild types and mutants were also estimated by analyzing the mean radius within the proper group. The results are shown in figure 6.10. First, the difference in mean radius values within the group of the 13E Cdk13 models was estimated to be 0.0643 mm (6.10 (A). The comparison of the E13 Cdk13 samples is shown in figure 6.10 (B). Mutant's radius was subtracted from the wild type's, resulting in 0.0084 mm. Lastly, the difference within the 15 days old Tmem 105 samples was determined (6.10 (C), and it's equal to 0.0259 mm.

Growth angle
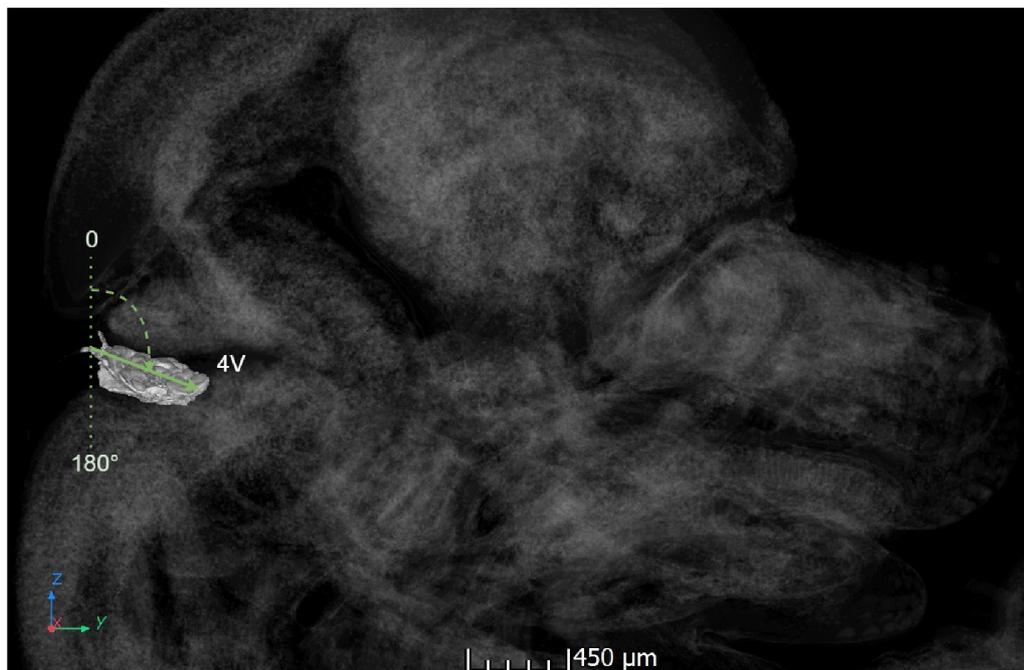
Fig. 6.11: An example of the growth angle of choroid plexus into the fourth ventricle (4V) represented by the dashed curved line between the direction vector (arrow) and Z=axis (dotted line). Sample: Cdk13 sample 6 Mut. View: sagittal plane.

The growth angle was determined as another quantitative feature of the choroid plexus. This feature represents the orientation of the choroid plexus into the fourth ventricle. Therefore, it brings knowledge about under which angle the plexus grows and extends into the ventricle. The angle was measured between the computed eigenvector of the model and the Z-axis. The example is shown in figure 6.11 where the dotted line represents the Z-axis, the arrow indicates the eigenvector, and the

curved dashed line stands for the growth angle. The eigenvector was determined by analyzing the 3D segmented model. The first eigenvector was chosen with the biggest variability and can be called the direction vector. All the measured angles are shown in figure 6.12. The blue bars indicate the obtuse angle and the red the acute angle. The plexus grows cranially with an acute angle and caudally with an obtuse angle. Cdk13 sample 2 WT showed the biggest angle, while Tmem 107 sample 3 WT had the smallest angle. All the Cdk13 samples have angles bigger than 90°. Most of the Tmem 107 samples had angles below 90° except two, Tmem 107 sample 1 WT and Tmem 107 sample 5 WT. These two samples were close to the right angle, 92° and 91°.
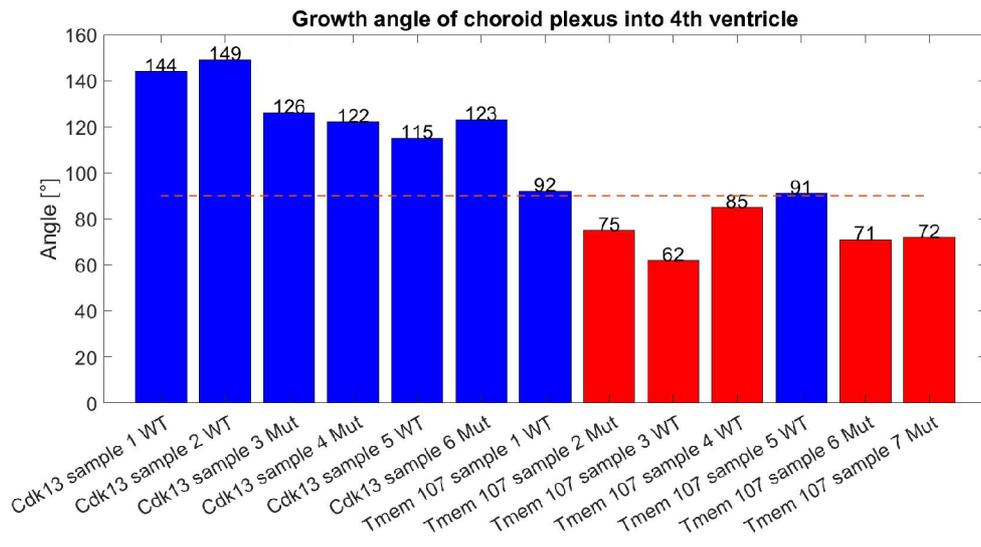
Fig. 6.12: Growth angles were measured for all 3D segmented models. The angle was measured between the direction vector and the Z-axis. The blue bars show the obtuse angle, and the red bars represent the acute angle. The red horizontal dashed line equals 90° and divides these two types of angles.

GPA

The shape analysis was achieved by investigating the location variances of selected landmarks among the segmented model. A landmark is a spot laced in the same region within the analyzed objects. Exactly six landmarks were chosen for the shape analysis: one on each branch extension to the foramen of Lushka, two on top of the area between the MHS and RSS, and two on the bottom of this location (figure 5.1). Landmarks were manually selected within each sample. The landmarks were further analyzed using generalized Procrustes analysis (GPA). Firstly, the optimal

mean shape was estimated. The shape was iteratively optimized by computing the differences between the calculated mean shape and the other models. The first model was selected as an initial mean shape. The optimization ended when the error value was under a specific threshold (=0.01). The error was calculated as the distance between the estimated shape i and i-1, where i is the current iteration number. The error plot is shown in figure 6.13, where the error value (=0.0066) was after the third iteration below the threshold.
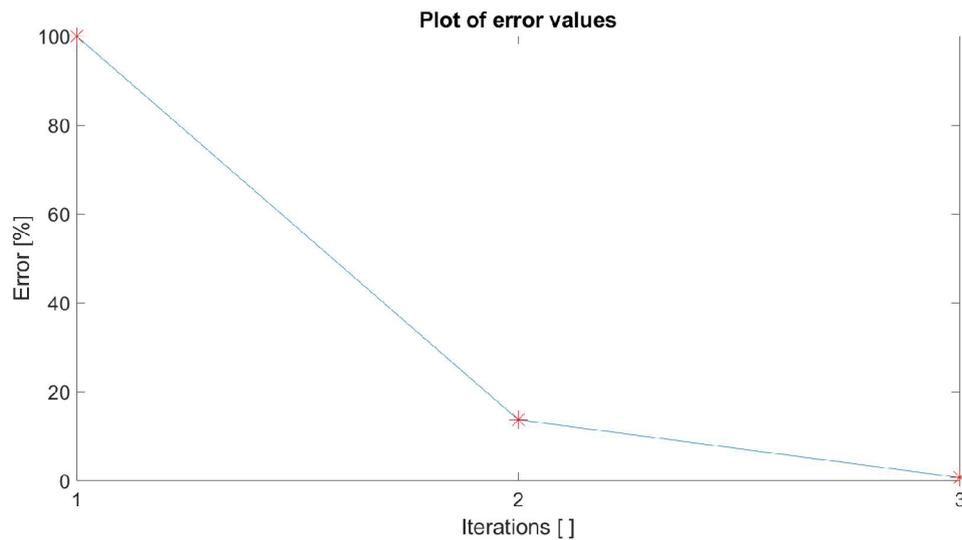
Fig. 6.13: Error between estimated shape and other shapes was computed after each iteration in GPA. The algorithm stops, once the error is below a threshold. In most cases, two iterations should suffice, according to Bookstein [5]

The landmark points were geometrically transformed to the optimal centre once the optimized mean shape model. Then, the scale and rotation matrix was computed using the estimated mean shape. Transformed landmark points and mean shape points are shown in figure 6.14. It is possible to see that the landmarks were aligned to the derivated mean model.
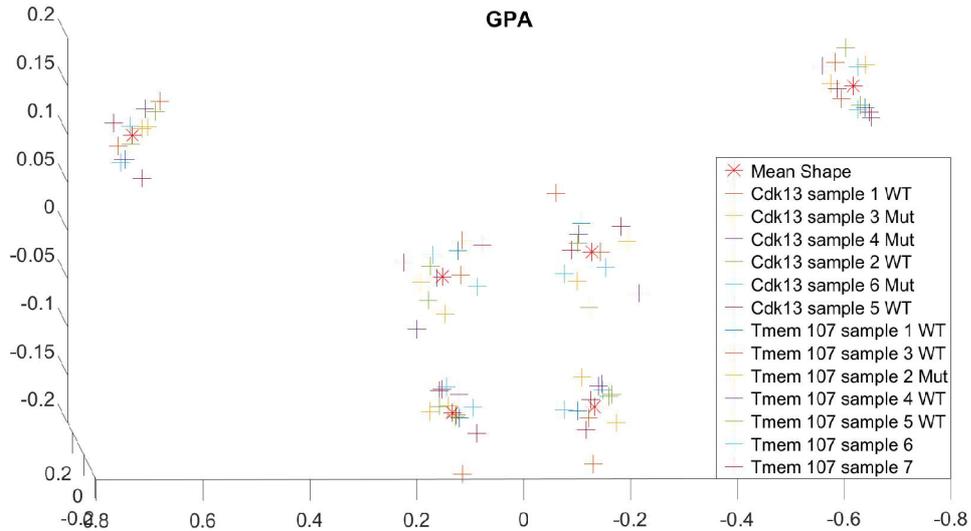
Fig. 6.14: The GPA result shows each sample's aligned landmark points to the mean shape. The alignment was done using the geometrical transformations.

The Procrustes distances were computed as the sum of the squared differences between each model and the mean shape model using the following equation:

$$Procrustes\_distance = \sum_{i=1}^{k}(mean\_shape\_model_i - Landmark_i)^2 \qquad (6.1)$$

where i is the i-th landmark point, k is the total number of landmarks of selected model. The resulting Procrustes distances are shown in figure 6.15.

The biggest distance was counted for Cdk13 sample 4 Mut, followed by the Cdk13 sample 1 WT with the second biggest value, 0.034 and 0.032, respectively. Both of these samples are from the E13 Cdk13 embryos. Finally, Tmem 107 sample was estimated 1 WT equal to be the closest sample to the mean shape, with Procrustes distance equal to 0.007. The biggest distance among the E15 Tmem 105 samples was 0.019 sample number 7. The wild type sample of the E15 Cdk13 group has shown a bigger distance than the mutant from its group, 0.017 and 0.014, respectively. Overall, the mean distance between mean shape and mutants was higher than for the wild types, 0.0173 and 0.0149.

The Procrustes distances were estimated between each pair of the samples. The distance was counted as the sum of squared differences between the transformed landmarks of the two models. For example, the biggest value was calculated between Cdk13 sample 4 Mut and Tmem 107 sample 4 WT. In contrast, the closest models were samples 4 and 5 from Tmem 107 group. Then the mean Procrustes distances were estimated using the computed distances for each pair of models within and between their categories. The highest mean Procrustes distance between pairs of

samples of the same or different kinds was between mutants, while the lowest was between wild types. The results for within-group analysis are shown in table 6.3. The mean distance between mutant models was lowest for the E13 Cdk13 group and highest for E15 Tmem 105 group. However, the E15 Tmem 105 wild type models are statistically closer and thus more similar in shape.
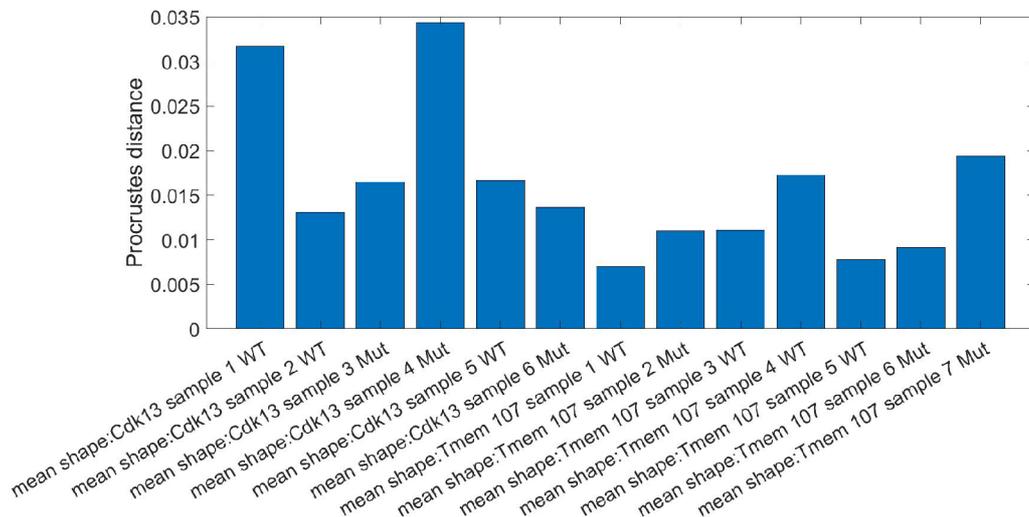
Fig. 6.15: The Procrustes distances were computed between the estimated mean shape and individual samples.

Tab. 6.3: The Procrustes distances between each pair of models were estimated within groups of samples. The mean distance was computed between wild type samples (WT:WT), mutants (MUT:MUT), and lastly, between both kinds (WT:MUT).

	mean distance WT:WT	mean distance WT:MUT	mean distance MUT:MUT
E13 Cdk13	0.0399	0.0440	0.0274
E15 Cdk13	-	0.0120	-
E15 Tmem 105	0.0196	0.0210	0.0256

The Procrustes distances between each pair of samples were further analyzed by hierarchical clustering shown in figure 6.16. This method was used to visualize the relations between the models given by their Procrustes distances. As a result, the graph was divided into four main clusters. One sample, Cdk13 sample 1 WT, was not assigned to any group, because of having the least similar shape to other models. The first cluster (purple) consists of only Tmem 105 models, where samples had the least distance with a sample of their kind. The second cluster (blue) reveals

the similarity between mutant and wild type samples from Cdk13 and Tmem 107 groups. The third cluster comprises two subclusters, where two different types of E15 Cdk13 models and two Tmem 105 wild type models were joined. Lastly, two mutant samples of Cdk13 are creating the fourth cluster.
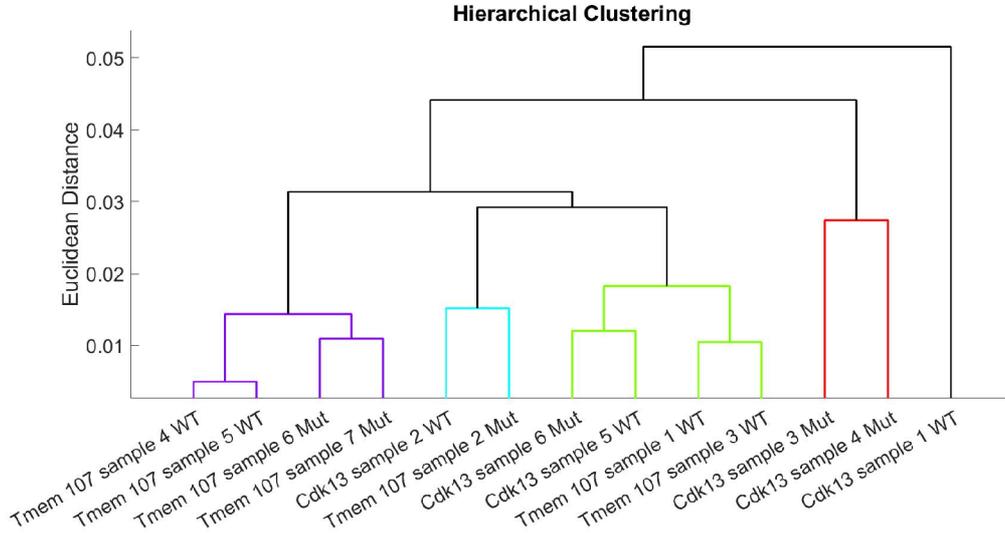
Fig. 6.16: The cluster analysis of aligned landmarks with parameters estimated by GPA. The Euclidean distance was computed between each sample. The graph shows four clusters (purple, blue, green, red) and one unclassified sample.

At last, the transformed landmarks from GPA were statistically interpreted by PCA to study the variety of the model shapes. First, the transformed landmark points were reshaped to form a matrix where each row corresponded to a model and column to the landmark's coordinate. Then, the matrix was normalized by subtracting the mean value. Figure 6.17 shows the results of the PCA and its first two principal components, which are modelling the shape variations among the samples. The first and second principal components explain 62% of the variability. The second principal component separates the data into two groups. The transformed points into the principal component's dimension were further studied with k-means clustering, creating 2 clusters.

The clustering enhanced the visualization of the sample distribution. It is possible to see that cluster number one contains all the Cdk13 samples (figure 6.17). Two Tmem 107 samples are also included in the first cluster and are divided among the PC1. Other Tmem 107 samples are within the second cluster. Cdk13 models 1 and 4 are located further from the centroid, which justifies their difference from the other samples. Examining the thirteen-days-old samples, the Cdk13 sample 1 is located away from other models in its class, pinpointing the contrast of this sample

from other E13 Cdk13 models. Compared to the hierarchical clustering (6.16), the Tmem samples from the purple group are found in the second cluster. However, the other Tmem models within the blue and the green group are not included in the second cluster except sample 1. Samples 2 and 3 are located in the first cluster, near the Cdk13 models from the hierarchical clustering (blue and green groups). The Cdk13 models from the red groups and Cdk13 sample 1 are positioned away from the centroid, proving their difference from the other models. Two clustered Cdk13 models from the green group are found in a close position within the space of the first and second principal components. Thus the PCA roughly confirms the hierarchical clustering.
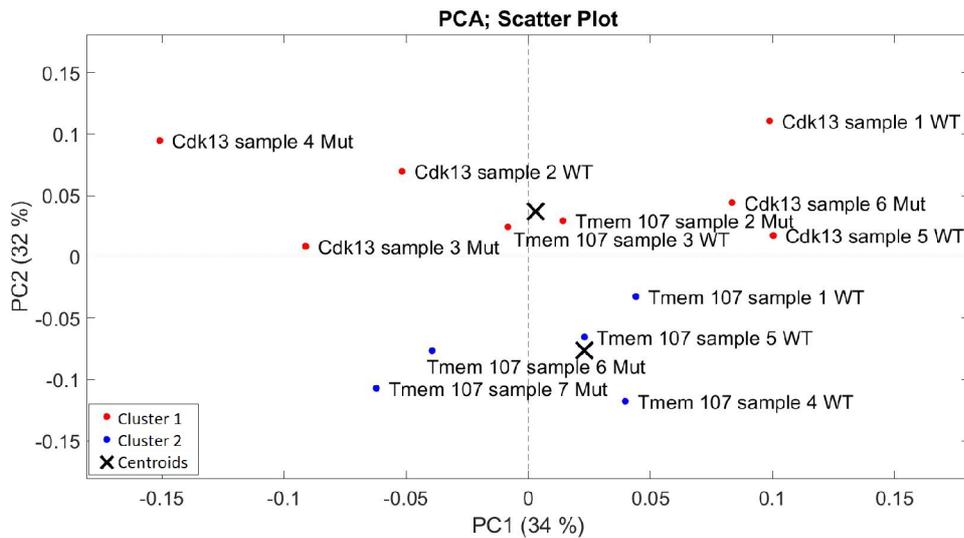
Fig. 6.17: PCA Scatter Plot. The aligned landmarks from GPA were statistically evaluated with PCA. The points were transformed into a principal components space showing the differences among the samples. The cluster analysis was further applied to distinguish the groups of points formed along the principal components.

6.2.1 Results summary

The morphological analyses and their results will be summarized in this section to determine whether there is a connection between the type of the sample and its morphological features. The choroid plexus grows differently among organisms. Thus, it was expected to have different parameters for each model [22].

The results will be compared between groups (Cdk13, Tmem 105), 13 (E13) and 15-days old (E15) embryos and between mutants and wild types. Firstly it was shown that all the E13 Cdk13 models have detached branches, except one

wild type model, in the RSS and miss the extension into the foramen of Luschka. Furthermore, the E15 Cdk13 mutant was missing both as the only 15-days old sample. Secondly, the volume and surface area showed their values are proportional as had been expected ([25]). Overall E13 samples showed lower volume and surface values than E15. The Tmem group has a more significant volume and surface area than the Cdk13 group. Figure 6.9 showed the mean values among the wild types and mutants for different group types and embryo age. Cdk15 samples showed a bigger mean value for wild types, while mutants had a bigger mean volume and surface area within the Tmem group.

Furthermore, volume and surface area do not differ significantly between mutants and wild types. However, the smallest value was measured for mutant samples, and the higher was seen for wild type model. Therefore, the sample type (mutant/wild type) and volume/surface area are not correlated.

Next, the growth angle was analyzed. The choroid plexus grows under an obtuse or acute angle. All Cdk13 samples have an obtuse growth angle, while the acute angle can be seen within the Tmem group except for two models, which are slightly over 90° (figure 6.12). Again, there is no significant difference between mutant and wild type growth angles.

Finally, the shape of segmented models was analyzed by alignment of the landmark points to the estimated mean shape. The Procrustes distance then showed the diversity of the models from the mean shape and between each other. Overall, the shapes are different among the samples of varying kinds and embryonic ages. E13 Cdk13 mutant and wild type showed the biggest distance from the mean shape, and the lowest was estimated for wild type from the Tmem group. The distance from the mean shape is higher within the mutants than for the wild type samples. Missing extensions caused it to the foramen of Luschka and unconnected branches of mutant models. A Comparison of each pair of models revealed a greater distance between mutants than wild-type models within the Tmem group. The E13 Cdk13 samples showed inverse results. At last, the clustering and PCA were performed to statistically evaluate the models' variety. The results showed the difference between Cdk13 and Tmem samples. Therefore, the models of the same group are initially clustered together in a cluster plot (6.16), except for one pair where the Cdk13 sample is clustered with the Tmem model. Overall, the cluster analysis did not show differences between wild types and mutants. The PCA divided the samples along the PC2 into Tmem (figure 6.17 blue) and the Cdk13 cluster (figure 6.17 red). However, there are two outliers from the Tmem group included in the Cdk13 cluster. Furthermore, the E13 Cdk13 models are more distant from the other models. Finally, PCA showed the relation between wild types and mutants within the Tmem group, where the samples of the same kind (mutant/wild type) are close.

Conclusion

The master's these aimed to study the morphological variations of the choroid plexus of the fourth ventricle within the micro CT data. An algorithm for segmentation of the choroid plexus was created to enable the analysis of its shape variations among the samples. Two types of samples were used with different gene alterations. Cdk13 and Tmem 107 genes were examined by comparing the wild types (WT) with the mutants. Morphological changes in the choroid plexus were seen during the preliminary studies of the Cdk13 gene, which motivated the project. Furthermore, a connection between Tmem 107 and choroid plexus was noted but never studied [44]. Consequently, the two types of models were compared for the morphological changes of the choroid plexus.

Firstly, the segmentation approaches were studied. Neural network methods showed excellent results, though there is a need for a training dataset of adequate size, which was not available for this project. Next, the GMM was introduced as another segmentation approach resulting in a promising tool for improving the initial segmentation of the choroid plexus as it uses prior knowledge about the ChP mask. Then, the region-based descriptor followed by a structured classifier was presented. The classification is done based on the extracted features from the regions. This method works well on clinical data, and multiple brain structures can be accessed with this segmentation. Next, the active contours were described for the choroid plexus segmentation. The initial point was manually selected in the data, which served as a starting point for the active contours algorithm. Furthermore, the methods describing the segmentation of the ventricle were presented. The segmentation of the ventricular region can enable the localisation of the choroid plexus within the imaging data. Model-guided, template matching methods and a method based on anatomical knowledge were proposed. Finally, all the segmentation methods were compared, and the resulting algorithm was created.

The segmentation algorithm works semiautomatically and uses knowledge about the location of the choroid plexus, which lies within the fourth ventricle. The fourth ventricle is extracted from data by searching for low intensity's biggest 3D connected region, representing the CSF. Initially, the plexus is segmented by thresholding the fourth ventricle area, followed by the active contours model. Next, the active contours model was used to access the entire region of the choroid plexus. Only a limiting number of iterations could be used as the mask started to leak out of the ChP region. The number was empirically estimated to be 100. Finally, the segmentation was corrected manually as the algorithm showed a limitation in segmentation of the lateral ChP, which extends into the foramen of Luschka. The missing ChP regions were added to the segmentation. The segmentation without the manual correction

showed an excellent ability to detect a choroid plexus within the micro CT data. However, some regions were not included in the segmentation caused of low contrast and missing boundaries between the ChP and the surrounding tissue.

The segmented models of choroid plexus were quantitatively and morphologically analyzed in the next part of the thesis. The analysis assessed the differences among the different types of samples (Cdk13, Tmem 107) and their kinds (mutants, wild types). Firstly, morphological aberrations were seen within some Cdk13 samples, where the extension to the foramen of Luschka was missing, and the two L-shaped branches of the choroid plexus were not connected in RSS. The aberrations were seen within all E13 Cdk13 samples and one E15 Cdk13 mutant sample. This shows that the choroid plexus is still developing at E13, which caused structure differences with other models. Next, segmented models' volume and surface area did not reveal a correlation between these features and sample kind(mutant/wild type). However, the smallest values were measured for a mutant sample and the biggest for the wild type. The Tmem 107 group exhibited higher volume and surface values than the Cdk13 and sample groups. Then, the growth angle of the choroid plexus into the fourth ventricle was determined and showed a difference between Cdk13 and Tmem 107 groups, where the angles were obtuse and acute, respectfully. Again, no significant difference between mutants and wild types was noticed by analyzing the growth angle. Lastly, GPA studied the segmented shapes, which aligned the manually selected landmark points with an estimated mean shape. Consequently, the Procrustes distances were measured between each sample and a mean shape and between each pair of models. E13 samples showed the biggest distance from the mean shape. This is caused by the fact that the plexus is still in development on the 13th day. Furthermore, the distance from the mean shape was higher for the mutants, which showed the difference with wild type models. Lastly, the PCA and clustering were performed to display the shape differences. The result demonstrated the difference between Cdk13 and Tmem 107 models as the models of the same groups were clustered together. In addition, PCA showed the shape variation between the mutants and wild types of the Tmem 107 group. Overall, the difference among the sample types and their kinds showed that the ChP morphology is affected differently by a Cdk13 and Tmem 107 gene knockout.

Bibliography

[1] ACHARYA, Anushree, Syed Irfan RAZA, Muhammad Zeeshan ANWAR, et al. Wolfram-like syndrome with bicuspid aortic valve due to a homozygous missense variant in CDK13. *Journal of Human Genetics.* 2021, **66**(10), 1009-1018. ISSN 1434-5161. doi:10.1038/s10038-021-00922-0

[2] *A new species of Halopteris (Hydrozoa: Leptothecata) and redescription of Plumularia rotunda from Victoria, Australia* [online]. 73. 2015 [cit. 2022-01-06]. ISSN 1447-2546.

[3] BAI, Xiangzhi, Fugen ZHOU and Bindang XUE. *Image enhancement using multi scale image features extracted by top-hat transform.* 2012, **44**(2), 328-336. ISSN 00303992. doi:10.1016/j.optlastec.2011.07.009

[4] BEDELL, Barry J. and Ponnada A. NARAYANA. Automatic segmentation of gadolinium-enhanced multiple sclerosis lesions. *Magnetic Resonance in Medicine.* 1998, **39**(6), 935-940. ISSN 07403194. doi:10.1002/mrm.1910390611

[5] BOOKSTEIN, Fred L. Landmark methods for forms without landmarks: morphometrics of group differences in outline shape. *Medical Image Analysis.* 1997, **1**(3), 225-243. ISSN 13618415. doi:10.1016/S1361-8415(97)85012-8

[6] CHAN, T.F. and L.A. VESE. Active contours without edges. *IEEE Transactions on Image Processing.* **10**(2), 266-277. ISSN 10577149. doi:10.1109/83.902291

[7] CHANG, P-C, K LIANG, JC LIM, M-C CHUNG, L-Y CHIEN and Emiliano SANTARNECCHI. A comparison of the thresholding strategies of micro-CT for periodontal bone loss: a pilot study. *Dentomaxillofacial Radiology.* 2013, **42**(2), 1057-1068. ISSN 0250-832X. doi:10.1259/dmfr/66925194

[8] CHEN, Vivian S., James P. MORRISON, Myra F. SOUTHWELL, Julie F. FOLEY, Brad BOLON and Susan A. ELMORE. Histology Atlas of the Developing Prenatal and Postnatal Mouse Central Nervous System, with Emphasis on Prenatal Days E7.5 to E18.5. *Toxicologic Pathology.* 2017, **45**(6), 705-744. ISSN 0192-6233. doi:10.1177/0192623317728134

[9] CHEN, Wenan, Rebecca SMITH, Soo-Yeon JI, Kevin R WARD, Kayvan NAJARIAN and Jing WANG. Automated ventricular systems segmentation in brain CT images by combining low-level segmentation and high-level template matching. *BMC Medical Informatics and Decision Making.* 2009, **9**(S1), 1-11. ISSN 1472-6947. doi:10.1186/1472-6947-9-S1-S4

[10] COOTES, T. F. and C. J TAYLOR. *Statistical Models of Appearance for Computer Vision.* University of Manchester, 2001. http://www.isbe.man.ac.uk/~bim/, oct 2001

[11] DORR, A.E., J.P. LERCH, S. SPRING, N. KABANI and R.M. HENKELMAN. High resolution three-dimensional brain atlas using an average magnetic resonance image of 40 adult C57Bl/6J mice. *NeuroImage.* 2008, **42**(1), 60-69. ISSN 10538119. doi:10.1016/j.neuroimage.2008.03.037

[12] DRYDEN, I.L. and K.V. MARDIA. *Statistical Analysis of Shape.* John Wiley Sons, Chichester, 1998.

[13] DUTA, Nicolae. Procrustes Shape Distance. *Encyclopedia of Biometrics.* Boston, MA: Springer US, 2015, 2015-7-3, 1278-1279. ISBN 978-1-4899-7487-7. doi:10.1007/978-1-4899-7488-4_864

[14] FINLAY, Barbara L. and Richard B. DARLINGTON. Linked Regularities in the Development and Evolution of Mammalian Brains. *Science.* 1995, **268**(5217), 1578-1584. ISSN 0036-8075. doi:10.1126/science.7777856

[15] HACKER, H. and H. ARTMANN. The calculation of CSF spaces in CT. *Neuroradiology.* 1978, **16**(1), 190-192. ISSN 0028-3940. doi:10.1007/BF00395247

[16] HAYMAN, LA, RA EVANS, VC HINCK, Tulika GUPTA, Marios LOUKAS, Daisy SAHNI, Shaheryar F. ANSARI and Aaron A. COHEN-GADOL. Choroid plexus of the fourth ventricle: a useful CT landmark. *American Journal of Roentgenology.* Cambridge: Cambridge University Press, 1979, **133**(2), 285-288. ISBN 9781139382816. ISSN 0361-803X. doi:10.2214/ajr.133.2.285

[17] HUANG, Ruobing, Ana NAMBURETE, Alison NOBLE and Philippe QUETIN. Learning to segment key clinical anatomical structures in fetal neurosonography informed by a region-based descriptor. *Journal of Medical Imaging.* IEEE, 2018, 2016, **5**(01), 1-4. ISBN 978-1-4673-9897-8. ISSN 2329-4302. doi:10.1117/1.JMI.5.1.014007

[18] HUBERT, Violaine, Fabien CHAUVEAU, Chloé DUMOT, Elodie ONG, Lise-Prune BERNER, Emmanuelle CANET-SOULAS, Jean-François GHERSI-EGEA and Marlène WIART. Clinical Imaging of Choroid Plexus in Health and in Brain Disorders: A Mini-Review. *Frontiers in Molecular Neuroscience.* 2019, **12**(8), 445-457. ISSN 1662-5099. doi:10.3389/fnmol.2019.00034

[19] JAN, Jiri. Medical Image Processing, Reconstruction and Analysis: Concepts and Methods. Second Edition.Boca Raton: CRC Press, 2019. ISBN 9781138310285.

[20] JOHANSSON, Pia A. The choroid plexuses and their impact on developmental neurogenesis. *Frontiers in Neuroscience.* 2014, **8**. ISSN 1662-453X. doi:10.3389/fnins.2014.00340

[21] JOLLIFFE, Ian T. and Jorge CADIMA. Principal component analysis: a review and recent developments. *Philosophical Transactions of the Royal Society A: Mathematical, Physical and Engineering Sciences.* 2016, **374**(2065). DOI: 10.1098/rsta.2015.0202. ISSN 1364-503X.

[22] KAISER, Karol, Ahram JANG, Petra KOMPANIKOVA, et al. *Development.* 2021, **148**(10). ISSN 0950-1991. doi:10.1242/dev.192054

[23] KENDALL, David G. A Survey of the Statistical Theory of Shape. *Statistical Science.* Institute of Mathematical Statistics, 1989, **4**(2), 87-99. ISSN 08834237.

[24] KOSZTOWSKI, Thomas A., Aristotelis S. FILIPPIDIS, C. Rory GOODWIN, Benjamin D. ELDER, Daniele RIGAMONTI and Daniele RIGAMONTI. Anatomy and physiology of the cerebrospinal fluid system. *Adult Hydrocephalus.* Cambridge: Cambridge University Press, 2014, **42**(1), 1-13. ISBN 9781139382816. ISSN 10538119. doi:10.1017/CBO9781139382816.002

[25] KÜHSEL, Sara, Adrian BRÜCKNER, Sebastian SCHMELZLE, Michael HEETHOFF and Nico BLÜTHGEN. Surface area-volume ratios in insects. *Insect Science.* 2017, **24**(5), 829-841. ISSN 16729609. doi:10.1111/1744-7917.12362

[26] LEHMANN, Gaetan, David LEGLAND, Petra KOMPANIKOVA, et al. Efficient N-Dimensional surface estimation using Crofton formula and run-length encoding. *The Insight Journal.* 2021, **148**(10). ISSN 2327-770X. doi:10.54294/wdu86d

[27] LEHTINEN, M. K., C. S. BJORNSSON, S. M. DYMECKI, R. J. GILBERTSON, D. M. HOLTZMAN and E. S. MONUKI. The Choroid Plexus and Cerebrospinal Fluid: Emerging Roles in Development, Disease, and Therapy. *Journal of Neuroscience.* 2013, **33**(45), 17553-17559. ISSN 0270-6474. doi:10.1523/JNEUROSCI.3258-13.2013

[28] LEV ,M.H., and R.G. GONZALES *Brain Mapping: The Methods (Second Edition).* Second. San Diego: Academic Press, 2002, 427-484. ISBN 9780126930191. doi:10.1016/B978-012693019-1/50019-8

[29] LIU, Jimin, Su HUANG, Volkau IHAR, Wojciech AMBROSIUS, Looi Chow LEE and Wieslaw L. NOWINSKI. Automatic Model-guided Segmentation of

the Human Brain Ventricular System From CT Images. *Academic Radiology.* 2010, **17**(6), 718-726. ISSN 10766332. doi:10.1016/j.acra.2010.02.013

[30] LUN, Melody P., Edwin S. MONUKI and Maria K. LEHTINEN. Development and functions of the choroid plexus—cerebrospinal fluid system. *Nature Reviews Neuroscience.* 2015, **16**(8), 445-457. ISSN 1471-003X. doi:10.1038/nrn3921

[31] METSCHER, Brian D. MicroCT for developmental biology: A versatile tool for high-contrast 3D imaging at histological resolutions. *Developmental Dynamics* [online]. 2009, **238**(3), 632-640 [cit. 2022-01-06]. ISSN 10588388. doi:10.1002/dvdy.21857

[32] METSCHER, Brian D. MicroCT for comparative morphology: simple staining methods allow high-contrast 3D imaging of diverse non-mineralized animal tissues. *BMC Physiology.* 2009, **9**(1). ISSN 1472-6793. doi:10.1186/1472-6793-9-11

[33] MUSA, Sarhan M. Matrices, Determinants, and Vectors. *Fundamentals of Technical Mathematics.* Elsevier, 2016, 2016, 221-259. ISBN 9780128019870. doi:10.1016/B978-0-12-801987-0.00008-3

[34] ORHAN, Kaan, Arda BÜYÜKSUNGUR, Anjali AGGARWAL, Tulika GUPTA, Marios LOUKAS, Daisy SAHNI, Shaheryar F. ANSARI and Aaron A. COHEN-GADOL. Fundamentals of Micro-CT Imaging: Review and anatomic study highlighting anatomical variations. *Micro-computed Tomography (micro-CT) in Medicine and Engineering.* Cham: Springer International Publishing, 2020, 2020-07-26, **26**(7), 27-33. ISBN 978-3-030-16640-3. ISSN 09675868. doi:10.1007/978-3-030-16641-0_3

[35] PERIN, Paola, Riccardo ROSSETTI, Carolina RICCI, et al. 3D Reconstruction of the Clarified Rat Hindbrain Choroid Plexus. *Frontiers in Cell and Developmental Biology.* Cambridge: Cambridge University Press, 2021, **9**(1), 1-13. ISBN 9781139382816. ISSN 2296-634X. doi:10.3389/fcell.2021.692617

[36] QIAN, Xiaohua, Jiahui WANG, Shuxu GUO and Qiang LI. An active contour model for medical image segmentation with application to brain CT image. *Medical Physics.* 2013, **40**(2). ISSN 00942405. doi:10.1118/1.4774359

[37] QIAN, Xiaohua, Yuan LIN, Yue ZHAO, Xinyan YUE, Bingheng LU and Jing WANG. Objective Ventricle Segmentation in Brain CT with Ischemic Stroke Based on Anatomical Knowledge. *BioMed Research International.* 2017, **2017**, 1-11. ISSN 2314-6133. doi:10.1155/2017/8690892

[38] REICH, David, Alkes L PRICE and Nick PATTERSON. Principal component analysis of genetic data. *Nature Genetics.* 2008, **40**(5), 491-492. DOI: 10.1038/ng0508-491. ISSN 1061-4036.

[39] SANDOR, Tamas, David METCALF, Young-Jo KIM, M-C CHUNG, L-Y CHIEN and Emiliano SANTARNECCHI. Segmentation of brain CT images using the concept of region growing: a pilot study. *International Journal of Bio-Medical Computing.* 1991, **29**(2), 133-147. ISSN 00207101. doi:10.1016/0020-7101(91)90004-X

[40] SCHULZ-MIRBACH, Tanja, Martin HESS and Brian D METSCHER. Sensory epithelia of the fish inner ear in 3D: studied with high-resolution contrast enhanced microCT. *Frontiers in Zoology.* 2013, **10**(1). ISSN 1742-9994. doi:10.1186/1742-9994-10-63

[41] SCIOLLA, Bruno, Matthieu MARTIN, Philippe DELACHARTRE and Philippe QUETIN. Segmentation of the lateral ventricles in 3D ultrasound images of the brain in neonates. *2016 IEEE International Ultrasonics Symposium (IUS).* IEEE, 2016, 2016, 1-4. ISBN 978-1-4673-9897-8. doi:10.1109/ULTSYM.2016.7728560

[42] SHENOY, SS and F. LUI. Neuroanatomy, Ventricular System. *StatPearls [Internet].* Treasure Island (FL): StatPearls Publishing, 2022. doi:30422527

[43] SHYLO, Natalia A., Kasey J. CHRISTOPHER, Alejandro IGLESIAS, Aaron DALUISKI and Scott D. WEATHERBEE. TMEM107 Is a Critical Regulator of Ciliary Protein Composition and Is Mutated in Orofaciodigital Syndrome. *Human Mutation.* 2016, **37**(2), 155-159. ISSN 10597794. doi:10.1002/humu.22925

[44] SHYLO, Natalia A., Elli EMMANOUIL, Dylan RAMRATTAN and Scott D. WEATHERBEE. Loss of ciliary transition zone protein TMEM107 leads to heterotaxy in mice. *Developmental Biology.* 2020, **460**(2), 187-199. ISSN 00121606. doi:10.1016/j.ydbio.2019.12.014

[45] SMITH, Lindsay I. *A tutorial on Principal Components Analysis.* 2002. URL: http://www.cs.otago.ac.nz/cosc453/student_tutorials/principal_components.pdf

[46] SPECTOR, Reynold, Richard F. KEEP, S. ROBERT SNODGRASS, Quentin R. SMITH and Conrad E. JOHANSON. A balanced view of choroid plexus structure and function: Focus on adult humans. *Experimental Neurology.* 2015, **267**, 78-86. ISSN 00144886. doi:10.1016/j.expneurol.2015.02.032

[47] STEGMANN, Mikkel B. A Brief Introduction to Statistical Shape Analysis. *Informatics and Mathematical Modelling, Technical University of Denmark, DTU.* 2002, **15**(1).

[48] STRAZIELLE, Nathalie, Jean-Francois GHERSI-EGEA, C. Rory GOODWIN, Benjamin D. ELDER, Daniele RIGAMONTI and Daniele RIGAMONTI. Choroid Plexus in the Central Nervous System: Biology and Physiopathology. *Adult Hydrocephalus.* Cambridge: Cambridge University Press, 2000, **59**(7), 561-574. ISBN 9781139382816. ISSN 0022-3069. doi:10.1093/jnen/59.7.561

[49] TADAYON, Ehsan, Beatrice MORET, Giulia SPRUGNOLI, Lucia MONTI, Alvaro PASCUAL-LEONE and Emiliano SANTARNECCHI. Improving Choroid Plexus Segmentation in the Healthy and Diseased Brain: Relevance for Tau-PET Imaging in Dementia. *Journal of Alzheimer's Disease.* 2020, **74**(4), 1057-1068. ISSN 13872877. doi:10.3233/JAD-190706

[50] Telano LN, Baker S. Physiology, Cerebral Spinal Fluid. 2021 Jul 9. In: StatPearls [Internet]. Treasure Island (FL): StatPearls Publishing; 2021 Jan–. PMID: 30085549.

[51] TESAŘOVÁ, M., T. ZIKMUND, M. KAUCKÁ, I. ADAMEYKO, J. JAROŠ, D. PALOUŠEK, D. ŠKAROUPKA and J. KAISER. Use of micro computed-tomography and 3D printing for reverse engineering of mouse embryo nasal capsule: Review and anatomic study highlighting anatomical variations. *Journal of Instrumentation.* Cham: Springer International Publishing, 2016, 2020-07-26, **11**(03), C03006-C03006. ISBN 978-3-030-16640-3. ISSN 1748-0221. doi:10.1088/1748-0221/11/03/C03006

[52] TUBBS, R. Shane, Mohammadali M. SHOJA, Anjali AGGARWAL, Tulika GUPTA, Marios LOUKAS, Daisy SAHNI, Shaheryar F. ANSARI and Aaron A. COHEN-GADOL. Choroid plexus of the fourth ventricle: Review and anatomic study highlighting anatomical variations. *Journal of Clinical Neuroscience.* Cambridge: Cambridge University Press, 2016, **26**(7), 79-83. ISBN 9781139382816. ISSN 09675868. doi:10.1016/j.jocn.2015.10.006

[53] WU, Dan and Jiangyang ZHANG. Recent Progress in Magnetic Resonance Imaging of the Embryonic and Neonatal Mouse Brain. *Frontiers in Neuroanatomy.* 2016, **10**. ISSN 1662-5129. doi:10.3389/fnana.2016.00018

[54] YING, Xiaoyou, Norman J. BARLOW, Maureen H. FEUSTON, I. ADAMEYKO, J. JAROŠ, D. PALOUŠEK, D. ŠKAROUPKA and J. KAISER.

Micro—Computed Tomography and Volumetric Imaging in Developmental Toxicology. *Reproductive and Developmental Toxicology*. Cham: Elsevier, 2017, 2017, **11**(03), 1183-1205. ISBN 9780128042397. ISSN 1748-0221. doi:10.1016/B978-0-12-804239-7.00063-9

[55] ZHAO, Li, Xue FENG, Craig H. MEYER and David C. ALSOP. Choroid Plexus Segmentation Using Optimized 3D U-Net. *2020 IEEE 17th International Symposium on Biomedical Imaging (ISBI)*. IEEE, 2020, 2020, 381-384. ISBN 978-1-5386-9330-8. doi:10.1109/ISBI45749.2020.9098443